*energies*

MDPI

*Article*

# Thermo-Mechanical Controls on Permeability in Deep Fractured-Porous Carbonates During Underground Gas Storage

**Zhen Zhai [1,2], Quan Gan [1,2], Yan Wang [3], Saipeng Huang [1,2], Yuchao Zhao [4], Limin Li [3], Mingnan Xu [5], Junlei Wang [6] and Sida Jia [1,2,*]**

[1] State Key Laboratory of Coal Mine Disaster Dynamics and Control, Chongqing University, Chongqing 400044, China
[2] School of Resources and Safety Engineering, Chongqing University, Chongqing 400044, China
[3] Chongqing Xiangguosi Underground Gas Storage Company Limited, Chongqing 401120, China
[4] Exploration and Development Research Institute, PetroChina Southwest Oil & Gasfield Company, Chengdu 610051, China
[5] State Key Laboratory of Geomechanics and Geotechnical Engineering, Institute of Rock and Soil Mechanics, Chinese Academy of Sciences, Wuhan 430071, China
[6] PetroChina Research Institute of Petroleum Exploration & Development, Beijing 100083, China
* Correspondence: jsd@cqu.edu.cn

**Abstract**

Deep fractured-porous carbonate reservoirs used for underground gas storage (UGS) experience simultaneous changes in temperature and effective stress during cyclic injection and withdrawal, so predicting permeability evolution is essential for evaluating long-term injectivity and deliverability. Using the Xiangguosi UGS as the engineering background, we measured steady-state gas permeability of three fractured-porous carbonate cores under representative conditions (20–80 °C; 15–35 MPa). Permeability decreases nonlinearly under coupled loading: changing temperature or effective stress alone typically reduces permeability by 30–70%, while the maximum reduction under concurrent increases in both variables exceeds 80% relative to the reference condition. An exponential model was fitted to quantify the decay parameter of permeability with effective stress (0.038–0.046 $MPa^{-1}$) and with temperature (0.016–0.020 $°C^{-1}$). In addition, the temperature-related exponential decay parameter decreases with increasing effective stress, because compliant fractures and larger pores are progressively pre-closed, weakening the permeability response to temperature. Finally, we propose a parsimonious separable exponential model that reproduces the measurements with a mean relative error below 12%, providing a practical constitutive relation for multiphysics simulations of UGS in fractured-porous carbonates.

**Keywords:** fractured-porous carbonates; temperature and stress coupling; permeability evolution; underground gas storage; exponential model

Check for updates

Academic Editor: Nikolaos Koukouzas

Received: 30 December 2025
Revised: 16 January 2026
Accepted: 19 January 2026
Published: 22 January 2026

**Copyright:** © 2026 by the authors. Licensee MDPI, Basel, Switzerland. This article is an open access article distributed under the terms and conditions of the Creative Commons Attribution (CC BY) license.

## 1. Introduction

Converting depleted gas reservoirs or salt caverns into underground gas storage (UGS) facilities helps meet seasonal peak-shaving demand and enhance natural gas supply security [1–4]. Among the available storage types, gas reservoir UGS has become a major focus because its geology is well constrained, and existing well patterns and surface facilities can be reused [5,6]. In southwestern China, the construction of large-scale UGS facilities has increasingly focused on deeply buried marine fractured-porous carbonate reservoirs [7,8]. These reservoirs exhibit complex THMC (thermal-hydro-mechanical-chemical) coupling

behaviors during frequent, high-rate injection-withdrawal cycles [9,10]. Specifically, the synergy between thermal fluctuations and effective stress perturbations directly dictates fracture-pore connectivity and reservoir deliverability [11,12]. While previous studies have addressed independent stress sensitivity [13–17], characterizing the joint permeability response through parsimonious coupling models remains a critical prerequisite for accurate field-scale numerical implementation [18,19].

During UGS operation, pore pressure and temperature in the vicinity of the wellbore and within the reservoir vary significantly in both time and space [9], whereas the regional in-situ stress field remains essentially stable over the engineering timescale. As a result, the effective stress borne by the reservoir skeleton fluctuates cyclically with each injection and withdrawal cycle. At the same time, the temperature difference between the injected gas and the formation induces thermoelastic and thermochemical responses in the rock-fluid system [10,20]. The combined action of effective stress and temperature exerts a direct control over a number of key processes, including fracture opening and closure, pore-structure evolution, temporal deterioration, and partial recovery of permeability. This makes it a pivotal factor for describing the evolution of reservoir injectivity and deliverability, as well as for assessing the long-term operational safety of UGS facilities [11,12,17,21]. The stress-related component of this permeability evolution has consequently been a central topic in previous studies.

With respect to permeability stress sensitivity, early experimental work mainly focused on sandstones and other complex lithologic reservoirs. These studies generally concluded that permeability decreases with increasing effective stress and can be described by exponential or power-law relationships [14–17]. In the context of carbonate reservoirs, Yan et al. [13] have reported that the permeability of fractured-porous cores exhibits a rapid and non-linear decrease at low effective stress levels. Conversely, at higher stress levels, the permeability undergoes a gradual decline. Distinct sensitivity coefficients are exhibited by different pore structures. Sun et al. [6] and Gou et al. [17] showed that systems with coexisting fractures and matrix pores commonly display moderate to strong stress sensitivity, which can further reduce injectivity and deliverability under multi-cycle injection and production operations. With advances in experimental testing and imaging techniques, quantitative characterization of permeability stress sensitivity in carbonates has shifted from simple empirical functions to frameworks that explicitly link pore structure, permeability, and effective stress. Sun et al. [11] showed that fracture morphology and skeletal stiffness can lead to noticeable differences in stress sensitivity. Yang et al. [18] further pointed out that fractured carbonate rocks under high-stiffness conditions are particularly sensitive to stress and tend to exhibit stronger nonlinear behavior. Mi et al. [16], Zivar et al. [15], and Haghi et al. [14] successively proposed empirical relations between permeability and effective stress that are suitable for numerical simulations. Pu et al. [19] used digital rock physics to simulate the evolution of porosity and permeability in fractured-porous networks under multiaxial stress states, providing additional insight into the mechanisms of stress-dependent flow. Overall, these studies clarify how permeability responds to effective stress and provide a range of empirical stress-permeability relations. However, because most experiments were conducted under isothermal or single-temperature conditions, they offer only limited insight into temperature-related effects.

Temperature changes not only modify fluid properties but also significantly affect the mechanical and flow behavior of rocks through thermal expansion, thermally induced cracking, and mineral reactions [22,23]. Tomás et al. [22] indicated that the initiation and evolution of high-temperature thermal fractures is one of the key mechanisms governing mechanical deterioration and permeability variation in rocks. Wang et al. [23] found that moderate heating can induce microfracture opening and increase permeability, whereas at

higher temperatures and over longer durations, heating may cause structural collapse and pore clogging, leading to permeability reduction. Zhai et al. [24] observed that the relative permeability of sandstone is sensitive to temperature and that heating can substantially enhance oil-phase flow capacity. In the context of UGS, previous studies have shown that permeability generally decreases during heating and increases during cooling, and exhibits hysteresis under repeated heating-cooling cycles [20]. Even moderate cyclic temperature variations on the order of several tens of degrees Celsius can cumulatively alter reservoir flow properties by changing rock-skeleton stiffness, inducing thermal fractures, and triggering local structural rearrangement [25]. These observations highlight a key gap: under realistic UGS conditions, where temperature and effective stress vary simultaneously, the coupled microstructural evolution of deep fractured-porous carbonate reservoirs and its impact on permeability remain poorly constrained.

Operational conditions that truly reflect UGS behavior involve simultaneous changes in temperature and effective stress. Against this background, some studies have begun to incorporate coupled temperature and stress effects into experiments and theoretical models. Gao et al. [12] demonstrated that multi-cycle effective stress perturbations cause continuous reductions in permeability and porosity in carbonate reservoirs, leading to substantial and partly irreversible damage to UGS injectivity and deliverability. Sun et al. [11] and Luo et al. [26] investigated the coupled responses of fractured-porous marine carbonates and deep lacustrine carbonates under combined temperature and stress loading and proposed empirical models. Using micro-imaging and fractal theory, Huang et al. [27] and Yang et al. [18] showed that the cooperative deformation of the pore skeleton and the vuggy pore network under stress is a key factor controlling the intensity and nonlinearity of macroscopic stress sensitivity. Temperature influences this process mainly indirectly, by modifying skeleton stiffness and fracture evolution. Nevertheless, studies on permeability evolution under coupled temperature and stress conditions still have several limitations. First, most experiments use sandstones, granites, or generic carbonate blocks, and systematic tests on deep fractured-porous carbonate reservoir cores under in-situ stress and temperature conditions remain scarce. Second, part of the existing work is conducted in high-temperature geothermal settings (typically > 200 °C), which differ markedly from the moderate 20–80 °C thermal disturbances experienced by UGS facilities. Third, structurally clear, easily calibrated permeability models that couple temperature and effective stress for field-scale numerical implementation are still lacking.

To bridge these gaps, this study presents a targeted investigation focusing on the Carboniferous fractured-porous carbonates of the Xiangguosi UGS (XGS-UGS). By conducting experiments on natural reservoir cores under a complete $T - \sigma_{eff}$ matrix (20–80 °C; 15–35 MPa), we aim to systematically quantify the coupled thermo-mechanical response of permeability and develop a parsimonious constitutive model that can be readily utilized for field-scale numerical simulations.

## 2. Materials and Methods

### 2.1. Experimental Samples

The reservoir samples tested in this study were collected from XGS-UGS in southwestern China. The storage reservoir consists of Carboniferous carbonates and is classified as a fractured-porous reservoir [8]. The structural trap of XGS-UGS is an approximately north-south-trending, belt-like feature, and reservoir permeability shows clear spatial heterogeneity (Figure 1). To compare seepage responses under coupled temperature and effective stress conditions, representative core intervals were selected from the northern, central, and southern parts of the reservoir based on well-log interpretation. These intervals are hereafter referred to as North, Middle, and South, respectively.

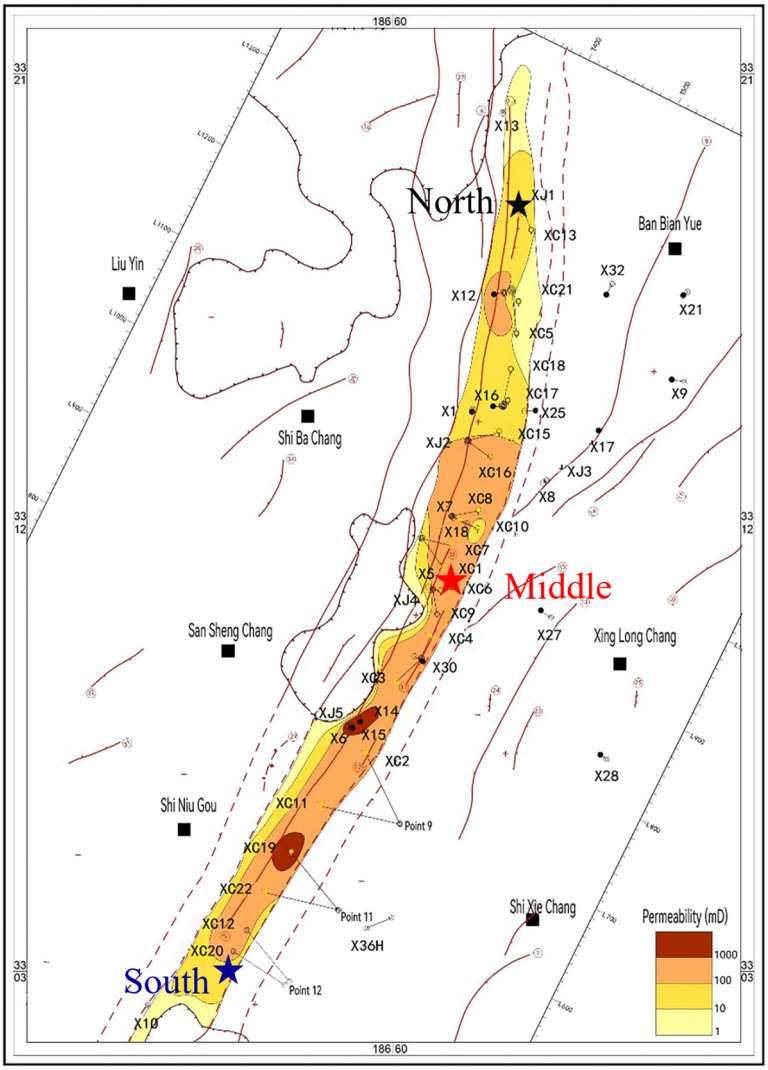


**Figure 1.** Plan-view permeability distribution of the Carboniferous carbonate reservoir in XGS-UGS and locations of the sampled core intervals (North, Middle, and South).

Sample preparation followed the Specifications for rock tests in water conservancy and hydropower engineering (SL/T 264-2020) [28] and the Standard for test methods of engineering rock masses (GB/T 50266-2013) [29]. Full-diameter cores were machined into cylindrical specimens with a diameter of 25 mm and a length of 50 mm. Dimensional tolerances and end-face flatness met the requirements of the standards. To provide a consistent preferential flow path among specimens, a throughgoing artificial fracture was introduced along the axial direction of each core using a diamond wire saw (Figure 2), which provides a simplified representation of a connected fracture pathway at the specimen scale. This treatment was designed to control the primary flow pathway and improve inter-specimen comparability, while acknowledging that it simplifies natural fracture complexity.

Before permeability tests, basic physical parameters of each specimen were measured (Table 1). Mineral composition was determined by powder X-ray diffraction (XRD) using a D8 ADVANCE diffractometer (Bruker, Karlsruhe, Germany). The XRD results show that the specimens are dolomite-dominated (65.0–100.0%). Quartz and calcite are mainly observed in the Middle specimen, whereas they are below the detection limit in the North and South specimens (Table 2), which is consistent with typical carbonate reservoirs.

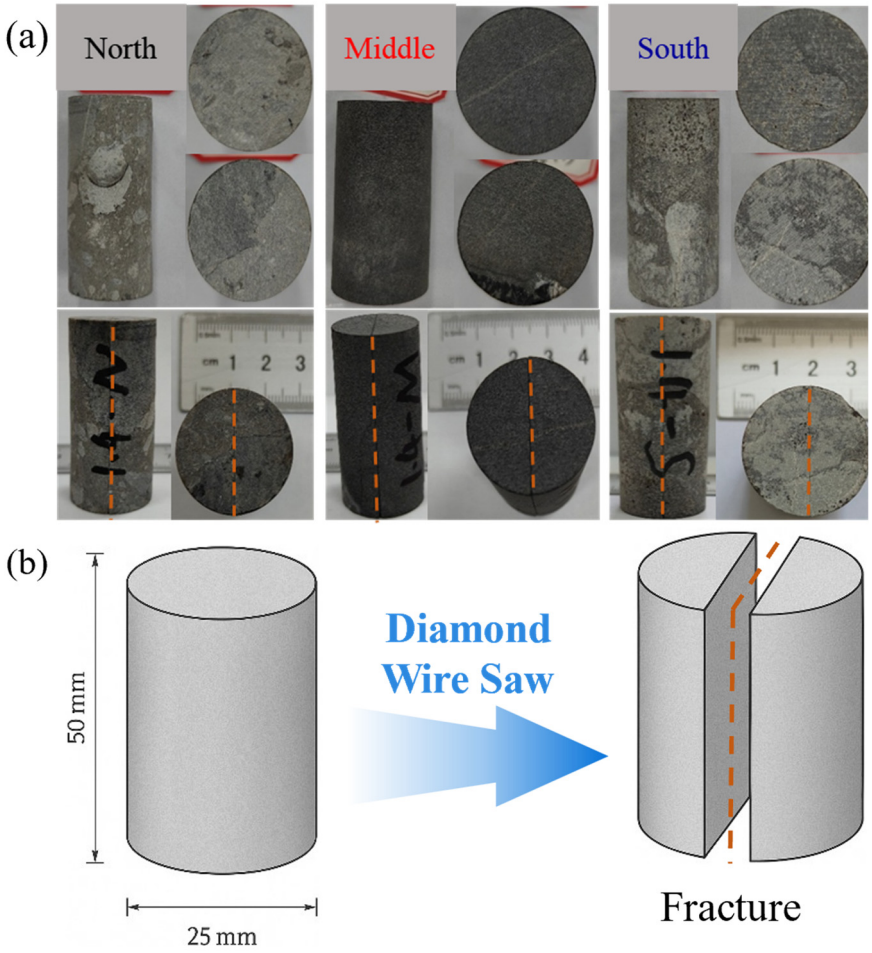


**Figure 2.** Photographs and schematic of specimen preparation: (**a**) representative core specimens from the North, Middle, and South intervals; (**b**) axial splitting using a diamond wire saw to create a throughgoing fracture.

**Table 1.** Basic information of the tested specimens.

| Sample ID | Sampling Horizon | Sampling Depth (m) | Length (mm) | Diameter (mm) | Mass (g) |
|---|---|---|---|---|---|
| North | Carboniferous | 2540.94–2541.11 | 50.00 | 25.10 | 64.566 |
| Middle | Carboniferous | 2352.11–2352.23 | 50.05 | 25.25 | 65.397 |
| South | Carboniferous | 2574.38–2574.54 | 50.00 | 25.15 | 63.473 |

**Table 2.** Mineral composition determined by powder XRD.

| Sample ID | Quartz (%) | Dolomite (%) | Calcite (%) |
|---|---|---|---|
| North | BDL | 100.0 | BDL |
| Middle | 21.4 | 65.0 | 13.7 |
| South | BDL | 100.0 | BDL |

Note: "BDL" indicates below the detection limit or trace amounts.

### *2.2. Experimental Apparatus and Permeability Calculation*

Permeability tests were conducted using a high-temperature and high-pressure gas-flow system (Figure 3). The system consists of a core holder, a confining pressure control unit, a gas injection unit, a temperature control unit, and a flow measurement unit (Figure 3a,b). The core holder (316L stainless steel) has an inner diameter of 25 mm and an adjustable length of 25–100 mm; it is rated to 50 MPa confining pressure and 180 °C. Gas injection was provided by a TC-300D constant-rate/constant-pressure pump (maximum

working pressure 70 MPa; accuracy ±1% full scale; flow rate range 0.0001–90 mL/min; cylinder volume 300 mL). To ensure that the specimen reached the preset temperature, five temperature sensors were installed at both ends and the middle of the specimen to monitor the core surface temperature in real time (Figure 3c).

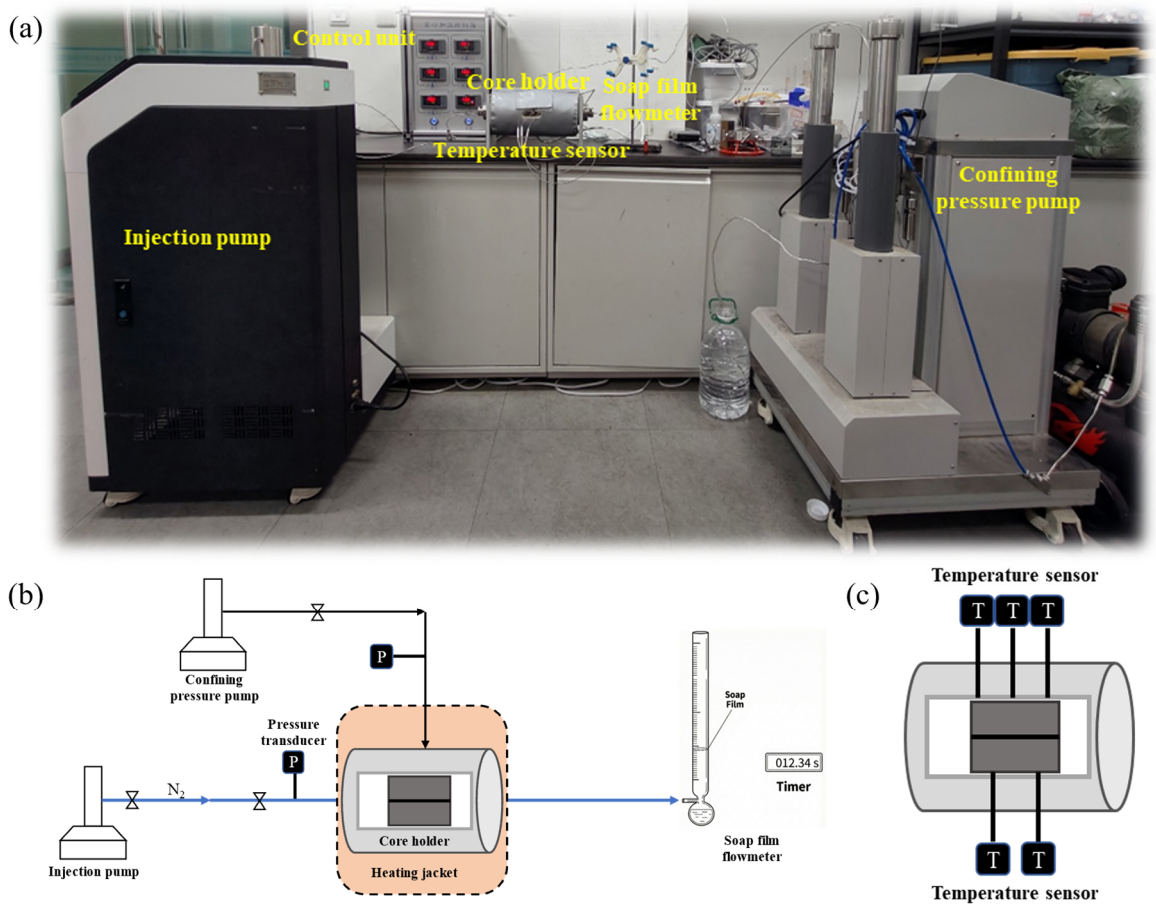


**Figure 3.** High-temperature and high-pressure gas-permeability apparatus: (**a**) photograph of the experimental setup; (**b**) schematic of the flow system; (**c**) layout of temperature sensors on the core holder.

The gas permeability measurements were conducted in strict accordance with the API RP 40 (Recommended Practices for Core Analysis) [30] and GB/T 29172-2012 (Practices for Core Analysis) [31] standards. A steady-state method was employed using high-purity nitrogen as the pore fluid. To account for the compressibility of gas, the permeability was calculated using the following integrated form of Darcy's Law for compressible flow [32–35]:

$$K = \frac{200 P_0 Q_0 \mu L}{A\left(P_1^2 - P_2^2\right)} \quad (1)$$

where $Q_0$ is the gas flow rate measured at the reference pressure $P_0$ (atmospheric pressure); $\mu$ is the gas viscosity at the test temperature [20,36,37]; $L$ and $A$ are the length and cross-sectional area of the core specimen, respectively; and $P_1$ and $P_2$ are the upstream (inlet) and downstream (outlet) pressures. By maintaining a constant pressure gradient across the specimen until the flow rate stabilized, the steady-state permeability was determined for each coupled temperature and stress condition.

Because this study focuses on the relative evolution of permeability with temperature and effective stress rather than absolute values, no Klinkenberg correction was applied. For fractured-porous specimens with permeabilities in the mD range, the slip-flow effect is sec-

ondary to the 30–80% reductions driven by thermo-mechanical loading. Furthermore, the use of normalized permeability ($K'$) largely mitigates systematic biases associated with gas slippage, as the effect remains relatively constant across the measured and reference states.

According to Biot's effective stress principle, the effective stress during the tests can be expressed as [15,38,39]:

$$\sigma_{eff} = \sigma_{tol} - \alpha P_p \quad (2)$$

where $\sigma_{eff}$ is effective stress (MPa); $\sigma_{tol}$ is total stress, which equals the confining pressure in this study (MPa); $\alpha$ is Biot's coefficient (0–1); and $P_p$ is pore pressure (MPa). In these experiments, the pore pressure ranged from 0.2 to 0.7 MPa. Within the confining pressure range of 15–35 MPa, the term $\alpha P_p$ contributes less than 5% of $\sigma_{eff}$ even when $\alpha$ = 1. While this approximation ($\sigma_{eff} \approx \sigma$) is numerically robust for calibrating parameters $C$ and $D$ under current laboratory conditions, it should be noted that in field-scale UGS operations, where pore pressure fluctuates significantly, the full effective stress term must be utilized to avoid systematic bias in predicting permeability evolution.

### 2.3. Experimental Procedures

Steady-state gas-flow tests were performed on three specimens at 20, 40, 60, and 80 °C. At each temperature, confining pressure was applied following predefined loading paths (Table 3). The overall workflow is shown in Figure 4.

**Table 3.** Test matrix and confining pressure loading paths.

| Sample | Pore Pressure (MPa) | Temperature (°C) | Confining Pressure Path (MPa) |
|---|---|---|---|
| North, Middle, South | 0.2–0.7 | 20 | 15→20→25→30→35 |
| | 0.2–0.7 | 40 | 15→25→35 |
| | 0.2–0.7 | 60 | 15→25→35 |
| | 0.2–0.7 | 80 | 15→25→35 |

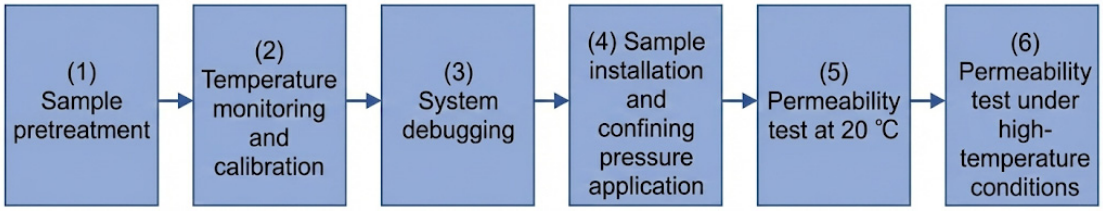


**Figure 4.** Workflow of the steady-state gas-permeability tests.

Tests at 20 °C. The gas-bottle pressure was adjusted, and the constant-rate/constant-pressure pump was started to supply $N_2$. The inlet pressure was regulated to maintain pore pressure within 0.2–0.7 MPa. Inlet pressure and volumetric flow rate were recorded every 10 min. Steady state was assumed when both pressure and flow rate varied by less than 5% over three consecutive measurements. After steady state was reached, three additional measurements were collected at 10 min intervals and averaged to calculate permeability using Equation (1). The confining pressure was then changed, and the above procedure was repeated to obtain permeability for the same specimen at effective stress levels of 15, 20, 25, 30, and 35 MPa.

Tests at elevated temperatures. For tests at 40, 60, and 80 °C, the target temperature was set, and the system was heated gradually while the core surface temperature was monitored in real time. Permeability testing started after the temperature stabilized at the target temperature for 1 h, with fluctuations not exceeding ±0.5 °C. At each elevated temperature, tests were performed at confining pressures of 15, 25, and 35 MPa, following the same steady-state criterion as at 20 °C.

## 3. Experimental Results

### 3.1. Permeability Test Data

The steady-state gas permeability results of the three specimens under all test conditions are summarized in Table 4. Under the reference condition ($T$ = 20 °C and $\sigma_{eff}$ = 15 MPa), the initial permeabilities of the North, Middle, and South specimens are 2.01, 2.95, and 1.13 mD, respectively, differing by a factor of approximately 2–3.

**Table 4.** Steady-state permeability of the three specimens under different temperatures and effective stresses.

| Temperature (°C) | Effective Stress (MPa) | Permeability of North (mD) | Permeability of Middle (mD) | Permeability of South (mD) |
|---|---|---|---|---|
| 20 | 15 | 2.01 | 2.95 | 1.13 |
| 20 | 20 | 1.45 | 2.33 | 0.91 |
| 20 | 25 | 1.16 | 1.88 | 0.73 |
| 20 | 30 | 0.97 | 1.56 | 0.60 |
| 20 | 35 | 0.80 | 1.32 | 0.50 |
| 40 | 15 | 1.08 | 1.56 | 0.64 |
| 40 | 25 | 0.83 | 1.27 | 0.51 |
| 40 | 35 | 0.66 | 1.08 | 0.42 |
| 60 | 15 | 0.86 | 1.27 | 0.53 |
| 60 | 25 | 0.58 | 0.94 | 0.43 |
| 60 | 35 | 0.46 | 0.79 | 0.36 |
| 80 | 15 | 0.61 | 0.98 | 0.46 |
| 80 | 25 | 0.47 | 0.82 | 0.38 |
| 80 | 35 | 0.39 | 0.70 | 0.33 |

Note: For T = 40–80 °C, tests were conducted at $\sigma_{eff}$ = 15, 25, and 35 MPa.

Such an initial difference is common for fractured carbonate cores and may reflect reservoir-scale heterogeneity as well as specimen-scale differences in fracture geometry. Previous studies suggest that flow in fractured-porous carbonates can be influenced by the connectivity between dissolution cavities (vug pores) and the fracture network, and that variations in fracture morphology or roughness may lead to substantial changes in measured permeability [18,27,40]. In this study, artificial fractures were prepared using the same wire-cutting procedure. However, variations in matrix fabric and cut surface micromorphology may still result in differences in fracture aperture and pore-fracture connectivity among specimens.

While these three representative cores (North, Middle, and South) capture the primary spatial heterogeneity of the XGS-UGS reservoir, they represent a localized population within a statistically larger and more complex geological system. Consequently, the measured permeabilities and subsequent sensitivity analyses should be viewed as indicative of the reservoir's behavior rather than an exhaustive characterization of all lithofacies present in the Carboniferous carbonate formation.

### 3.2. Permeability Variation with Effective Stress

Figure 5a shows the relationship between permeability and effective stress at $T$ = 20 °C for the three specimens. For all specimens, permeability decreases nonlinearly with increasing $\sigma_{eff}$, and the rate of decrease diminishes at higher stress. For example, the permeability of the North specimen decreases from 2.01 mD at 15 MPa to 0.80 mD at 35 MPa, corresponding to a reduction of approximately 60%. The corresponding reductions are approximately 55% for the Middle specimen (2.95 to 1.32 mD) and 56% for the South specimen (1.13 to 0.50 mD). These results demonstrate a marked dependence of permeability on effective stress within the tested range (15–35 MPa).

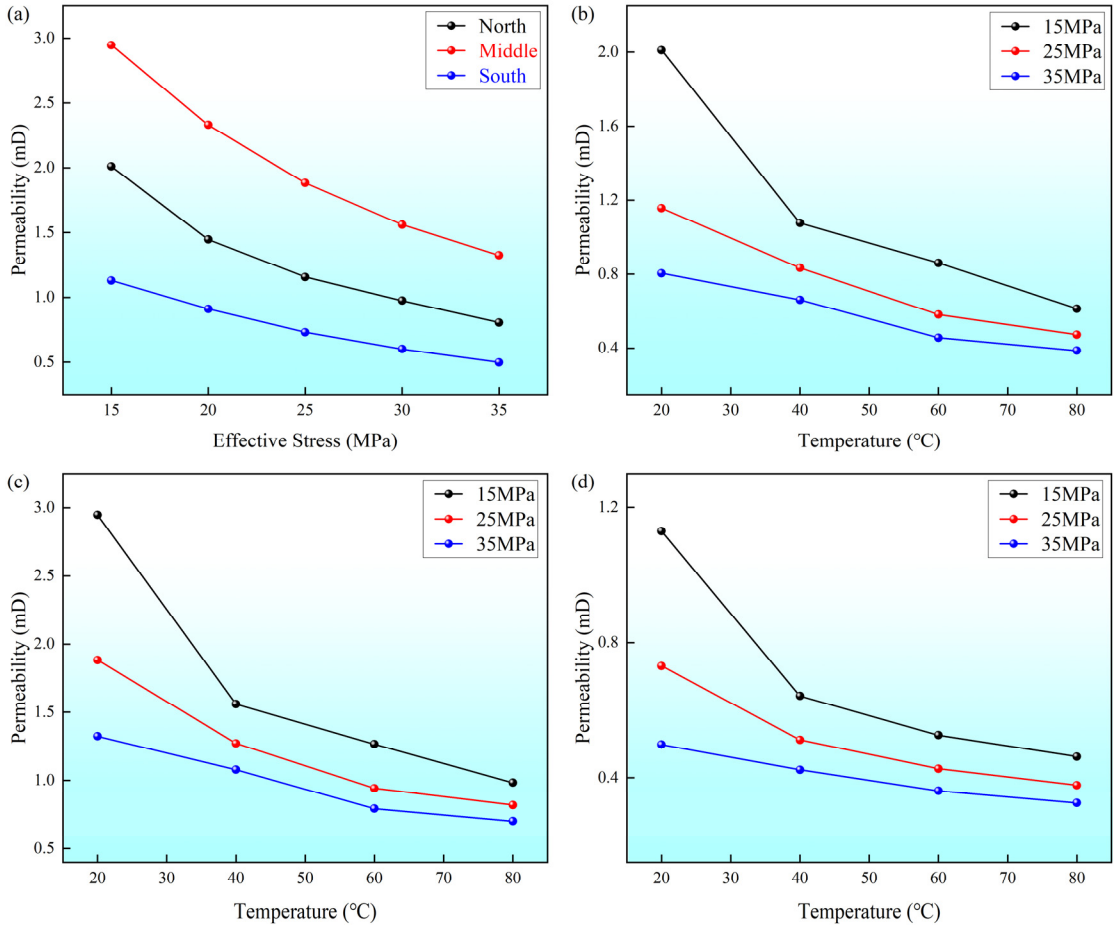


**Figure 5.** Permeability variations with effective stress and temperature. (**a**) Permeability versus effective stress at T = 20 °C for the three specimens. (**b**–**d**) Permeability versus temperature at $\sigma_{eff}$ = 15, 25, and 35 MPa for the North, Middle, and South specimens.

### *3.3. Permeability Variation with Temperature*

Figure 5b–d show permeability as a function of temperature at different effective-stress levels for the North, Middle, and South specimens. At a given $\sigma_{eff}$, permeability decreases with increasing temperature for all specimens. The trend is consistent across the tested stress levels, although the magnitude of reduction becomes smaller at higher $\sigma_{eff}$.

At $\sigma_{eff}$ = 15 MPa, increasing temperature from 20 to 80 °C reduces permeability from 2.01 to 0.61 mD for the North specimen (approximately 70%), from 2.95 to 0.98 mD for the Middle specimen (approximately 67%), and from 1.13 to 0.46 mD for the South specimen (approximately 59%). Considering all specimens together, the relative reductions over 20–80 °C are approximately 59–70% at 15 MPa, 48–59% at 25 MPa, and 34–51% at 35 MPa. These results indicate that permeability is clearly temperature-dependent within the investigated range, and that its temperature sensitivity is stronger at lower effective stress.

When temperature and effective stress vary simultaneously from the reference condition (20 °C, 15 MPa) to the combined condition (80 °C, 35 MPa), permeability decreases from 2.01 to 0.39 mD (North), from 2.95 to 0.70 mD (Middle), and from 1.13 to 0.33 mD (South), corresponding to reductions of approximately 81%, 76%, and 71%, respectively. This joint reduction highlights that both temperature and effective stress should be considered when evaluating permeability evolution under UGS-relevant operating conditions.

### *3.4. Normalized Permeability Representation*

To reduce the influence of inter-specimen differences in initial permeability and enable a consistent comparison of permeability variations under different testing conditions, dimensionless normalized permeability variables are introduced using a common reference state ($T_0$ = 20 °C, $\sigma_0$ = 15 MPa) Hereafter, the superscript prime ($\prime$) denotes normalized permeability.

To characterize the relative change in permeability with effective stress at the reference temperature $T_0$, the stress-normalized permeability is defined as:

$$K'_\sigma = \frac{K\left(\sigma_{eff}, T_0\right)}{K(\sigma_0, T_0)} \tag{3}$$

where $K'_\sigma$ is the dimensionless normalized permeability; $K\left(\sigma_{eff}, T_0\right)$ is the measured permeability at $T_0$ under a given effective stress $\sigma_{eff}$; and $K(\sigma_0, T_0)$ is the permeability at the reference condition $(\sigma_0, T_0)$. This normalization approach has been widely used in studies of stress sensitivity and permeability evolution [41,42], as it can substantially reduce the impact of inter-specimen variability in initial permeability and highlight the effect of effective stress on permeability. The resulting normalized trends are illustrated in Figure 6a. $K'_\sigma$ decreases monotonically and nonlinearly with increasing $\sigma_{eff}$ for all specimens.

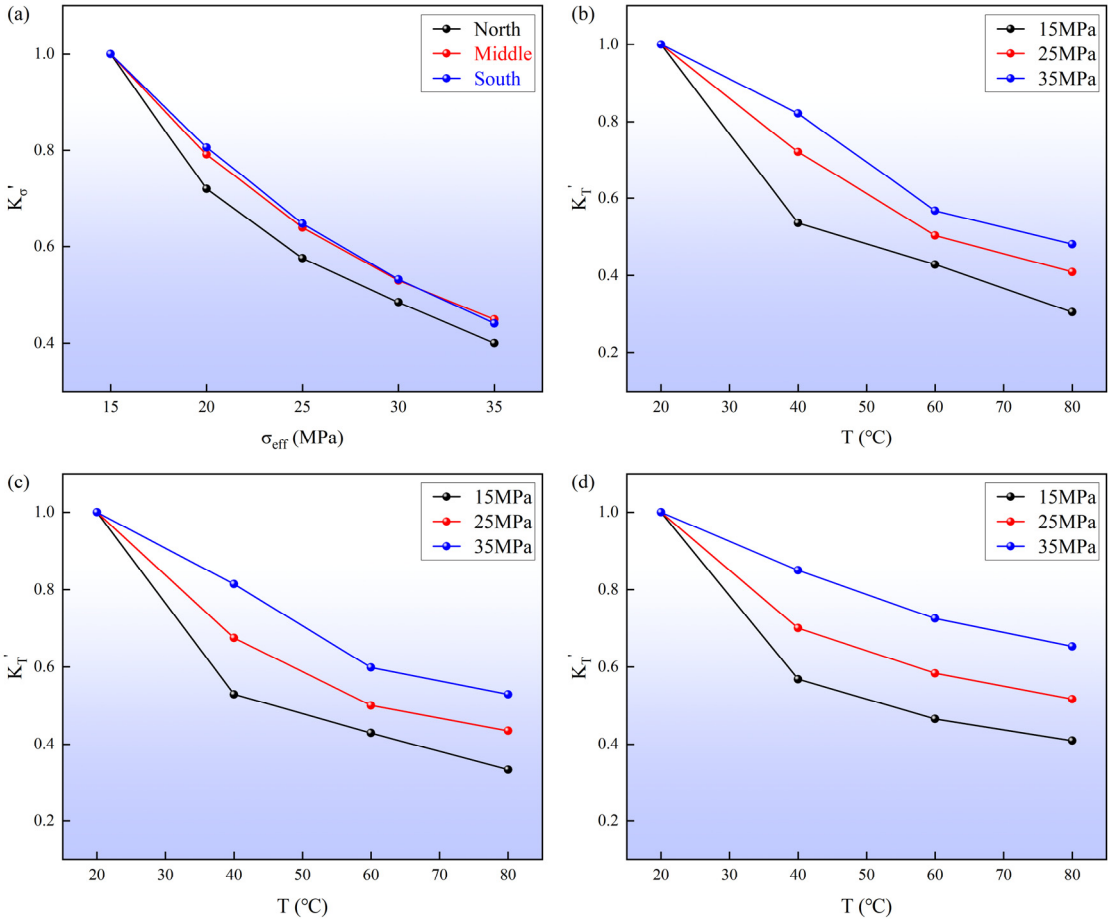


**Figure 6.** Normalized permeability results. (**a**) $K'_\sigma$ versus $\sigma_{eff}$ at $T_0$ = 20 °C for the three specimens. (**b**–**d**) $K'_T$ versus $T$ at $\sigma_{eff}$ = 15, 25, 35 MPa for (**b**) North, (**c**) Middle, and (**d**) South specimens.

To minimize the influence of different initial permeabilities on three specimens when examining temperature effects at a fixed effective stress, permeability is normalized by its value at the reference temperature $T_0$:

$$K'_T = \frac{K\left(\sigma_{eff}, T\right)}{K\left(\sigma_{eff}, T_0\right)} \tag{4}$$

where $K'_T$ is the dimensionless normalized permeability, $K\left(\sigma_{eff}, T\right)$ is the measured permeability at effective stress $\sigma_{eff}$ and temperature $T$, and $K\left(\sigma_{eff}, T_0\right)$ is the permeability at the same effective stress at $T_0$. The normalized results (Figure 6b–d) indicate that $K'_T$ decreases with increasing temperature for all specimens, while the magnitude of reduction becomes less pronounced at higher $\sigma_{eff}$.

For a unified representation of permeability data obtained under combined variations of effective stress and temperature, a coupled normalized permeability is further defined with respect to the same reference state:

$$K' = \frac{K\left(\sigma_{eff}, T\right)}{K(\sigma_0, T_0)} \tag{5}$$

where $K'$ is the dimensionless normalized permeability at a given $\left(\sigma_{eff}, T\right)$; $K\left(\sigma_{eff}, T\right)$ is the measured permeability; and $K(\sigma_0, T_0)$ is the permeability at the reference condition $T_0 = 20\ ^\circ\mathrm{C}$, $\sigma_0 = 15$ MPa. This coupled normalization enables permeability measurements acquired under different $\left(\sigma_{eff}, T\right)$ conditions to be compared within a unified dimensionless framework and will be used in the subsequent model development and validation.

## 4. Model Development

### *4.1. Model Scope, Assumptions, and Formulation Strategy*

This chapter develops an exponential, engineering-oriented permeability model for fractured-porous carbonate specimens under coupled variations of effective stress and temperature. To enable cross-specimen comparison and to reduce the influence of inter-specimen variability in initial permeability, we use the dimensionless normalized permeability variables defined in Section 3.4, including the stress-normalized permeability $K'_\sigma$, the temperature-normalized permeability $K'_T$, and the coupled normalized permeability $K'$. The model is intended to represent the experimental conditions investigated in this study (i.e., the effective stress and temperature ranges in Section 3), and its performance is assessed through systematic validation and error analyses.

The exponential model is constructed under the following assumptions, which are consistent with the experimental design and the intended use of the model within the tested range:

(1) Reference-state normalization. Differences among specimens in initial permeability are accounted for by normalization to $(\sigma_0, T_0)$ (Section 3.4), so that the model targets relative permeability changes rather than absolute values.
(2) Quasi-steady response at each loading step. The measured permeability at each imposed $(\sigma_{eff}, T)$ condition is treated as representative of an equilibrated state for modeling purposes; time-dependent effects are not explicitly modeled.
(3) No explicit microstructural evolution law. Changes in fracture roughness, asperity damage, and other microstructural evolutions are not parameterized explicitly; their

net influence is implicitly absorbed into fitted exponential parameters within the tested range.

(4) Separable stress and temperature effects (within the tested conditions). The coupled normalized permeability is approximated by a separable form,

$$K'\left(\sigma_{eff}, T\right) = f\left(\sigma_{eff}\right)g(T) \tag{6}$$

so that explicit cross-terms (e.g., $\left(\sigma_{eff} - \sigma_0\right)(T - T_0)$) are not included in the model. This separability assumption is grounded in the fundamental theory of fluid mechanics, where the hydraulic transmissivity of fracture-pore networks can often be decomposed into independent mechanical and thermal response functions under moderate loading conditions [43]. Similar simplifications have been successfully adopted in thermo-elastic-hydraulic modeling of tight sandstones and granites to balance computational efficiency with predictive accuracy [14,15,44]. This parsimonious form captures the primary thermo-mechanical evolution while avoiding the computational complexity associated with higher-order cross-terms. The separability assumption (Equation (6)) implies that the coupled permeability response can be approximated by the product of independent stress and temperature functions without explicit cross-terms. This approach is quantitatively justified by the subsequent error analysis (Section 4.5), which reveals a mean relative error of approximately 11–12% for the tested range. Within the moderate operating envelope of 20–80 °C and 15–35 MPa, this parsimonious form captures the primary thermo-mechanical evolution while avoiding the computational complexity and calibration challenges associated with higher-order coupling terms.

(5) Moderate-temperature regime. The investigated temperature range (20–80 °C) is treated as the applicability range of the proposed exponential model.

Within this framework, exponential expressions are adopted because they are widely used in permeability-stress or temperature studies and provide strictly positive predictions with a minimal number of parameters, facilitating stable calibration and sensitivity quantification. Based on this strategy, we first calibrate a stress model to obtain the stress-related exponential decay parameter $C$ (Section 4.2), then calibrate a temperature model to obtain the temperature-related exponential decay parameter $D$ (Section 4.3), and finally combine them into a coupled separable expression for prediction and validation (Sections 4.4 and 4.5).

### *4.2. Fitting of the Stress-Related Exponential Decay Parameter*

As shown in Figure 6a, $K'_\sigma$ decreases nonlinearly with increasing $\sigma_{eff}$ for all three specimens. This curve shape is consistent with the exponential type trends commonly reported for tight and fractured rock [45,46]. Therefore, an exponential model is adopted to fit the normalized data:

$$K'_\sigma = \exp\left[-C\left(\sigma_{eff} - \sigma_0\right)\right] \tag{7}$$

where $\sigma_0$ = 15 MPa is the reference effective stress, and $C$ (MPa$^{-1}$) is the stress-related exponential decay parameter. The parameter $C$ directly reflects how sensitive the permeability is to changes in effective stress and has a clear physical meaning [47,48].

The fitting results are presented in Figure 7a–c and Table 5. For all three cores, the goodness-of-fit $R^2$ is greater than 0.97, suggesting that Equation (7) provides a reasonable description of the stress-dependent decay in permeability over 15–35 MPa. The fitted $C$ values for the North, Middle and South cores are 0.0506, 0.0424 and 0.0420 MPa$^{-1}$.

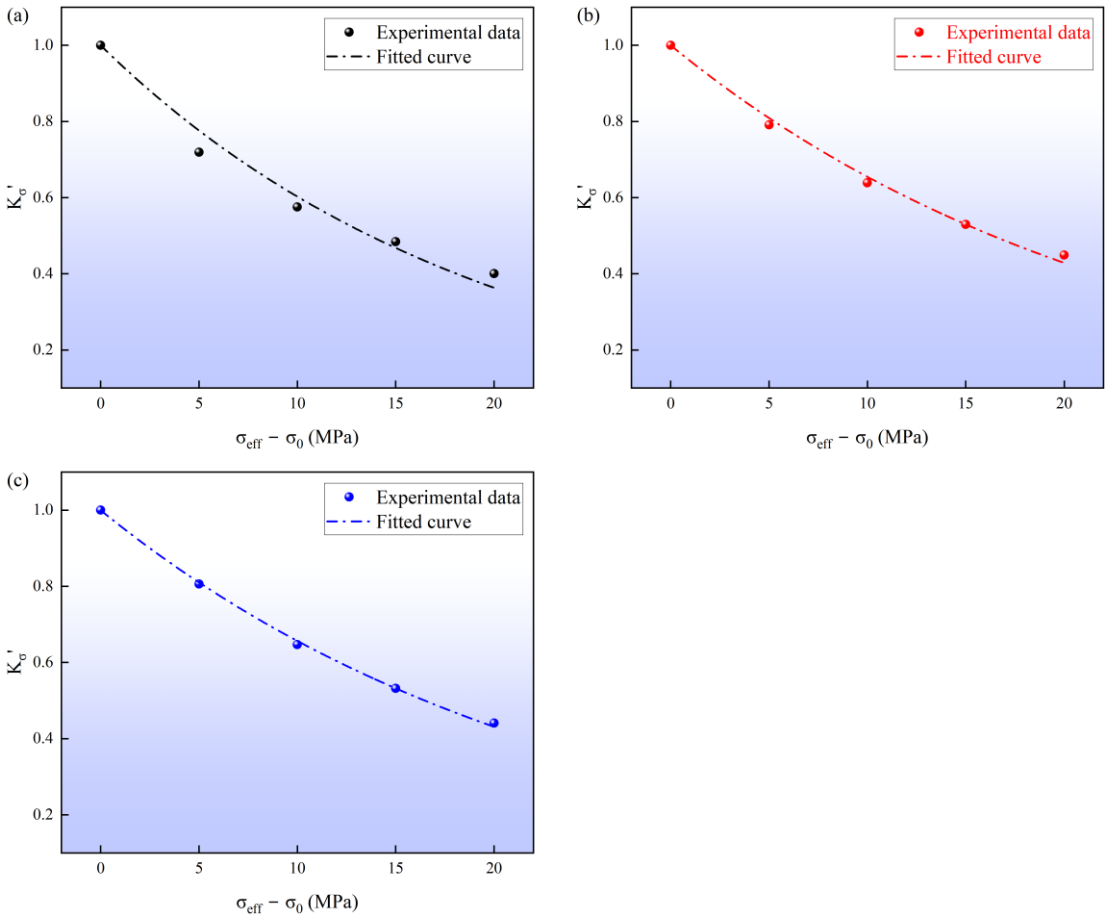


**Figure 7.** Normalized permeability exponential fitting results. (**a**–**c**) Experimental data and fitted curves for the North, Middle, and South cores.

**Table 5.** Fitted parameters of the exponential stress-sensitivity model (Equation (7)) at $T$ = 20 °C.

| Sample | Temperature (°C) | Model Form | $C$ (MPa$^{-1}$) | $R^2$ |
|---|---|---|---|---|
| North | 20 | $K'_\sigma = \exp\left[-C\left(\sigma_{eff} - \sigma_0\right)\right]$ | 0.0506 ± 0.0030 | 0.9746 |
| Middle | 20 | | 0.0424 ± 0.0011 | 0.9948 |
| South | 20 | | 0.0420 ± 0.0005 | 0.9990 |

### *4.3. Fitting of the Temperature-Related Exponential Decay Parameter*

As shown in Figure 6b–d, $K'_T$ decreases monotonically and nonlinearly with increasing temperature for all three cores at each effective stress. Previous work has shown that, within the mid to low temperature range, the permeability-temperature relationship can often be captured by an exponential-type model [22]. In this sense, the parameter $D$ can be interpreted as an experimental indicator that integrates the combined effects of thermoelastic expansion of the pore skeleton and microstructural adjustment. Similar formulations have also been widely adopted to characterize temperature-dependent permeability in low-permeability sandstones [44,49]. Referring to the exponential functions commonly used in studies of rock temperature-permeability coupling, the relationship between $K'_T$ and $T$ is fitted as

$$K'_T = \exp[-D(T - T_0)] \quad (8)$$

where $T_0$ = 20 °C is the reference temperature and $D > 0$ (°C$^{-1}$) is the temperature-related exponential decay parameter, representing the relative decay rate of permeability per Celsius increase with respect to $T_0$.

Here, $D$ is fitted separately at each $\sigma_{eff}$ to evaluate the influence of effective stress on the temperature sensitivity of permeability. The coupled model in Section 4.4 adopts constant $C$ and $D$ to couple temperature and effective-stress effects via a parsimonious separable exponential form.

The fitted curves (Figures 8–10) and Table 6 show that the exponential decay model provides a satisfactory description of the data. For all test conditions, the goodness-of-fit $R^2$ is greater than 0.90 and, in most cases, exceeds 0.95, confirming the applicability of Equation (8) to the 20–80 °C temperature conditions relevant to UGS engineering. The fitted temperature-related exponential decay parameter $D$ mainly falls in the range of 0.0075–0.023 °C$^{-1}$. As illustrated in Figures 8–10, the exponential decay model accurately captures the nonlinear reduction of permeability with temperature across all tested stress levels. A key feature of these plots is the systematic change in the curvature: the curves are steepest at the lowest effective stress (15 MPa) and become significantly flatter as the stress triples to 35 MPa. This visual 'flattening' directly reflects the decline in the temperature-related decay parameter $D$ (Table 6).

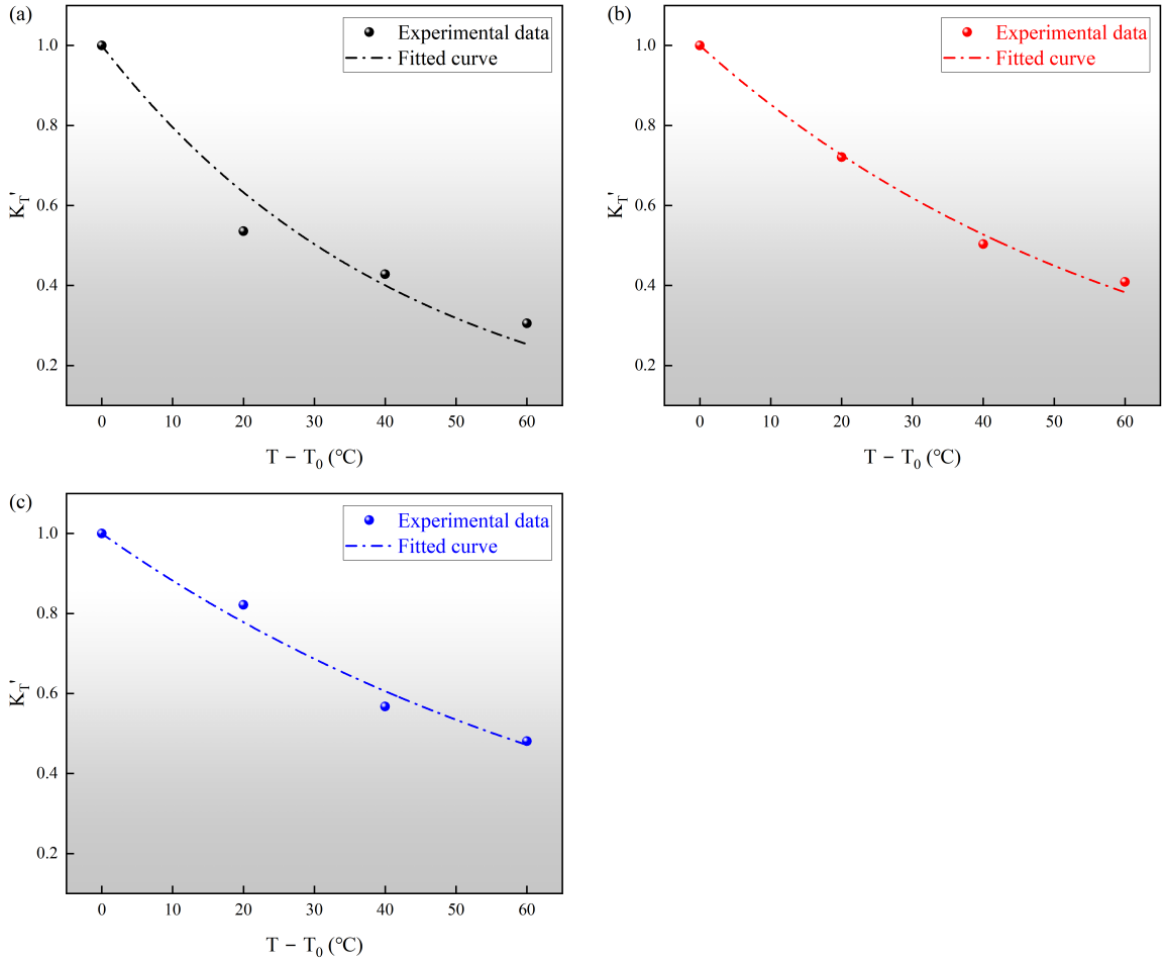


**Figure 8.** Exponential fitting of normalized permeability ($K_T'$) versus temperature for the North core under different effective stresses: (**a**) 15 MPa; (**b**) 25 MPa; and (**c**) 35 MPa. The progressive flattening of the fitted curves at higher stress levels illustrates the mechanical 'passivation' of the thermal response as compliant conduits are pre-closed by effective stress.

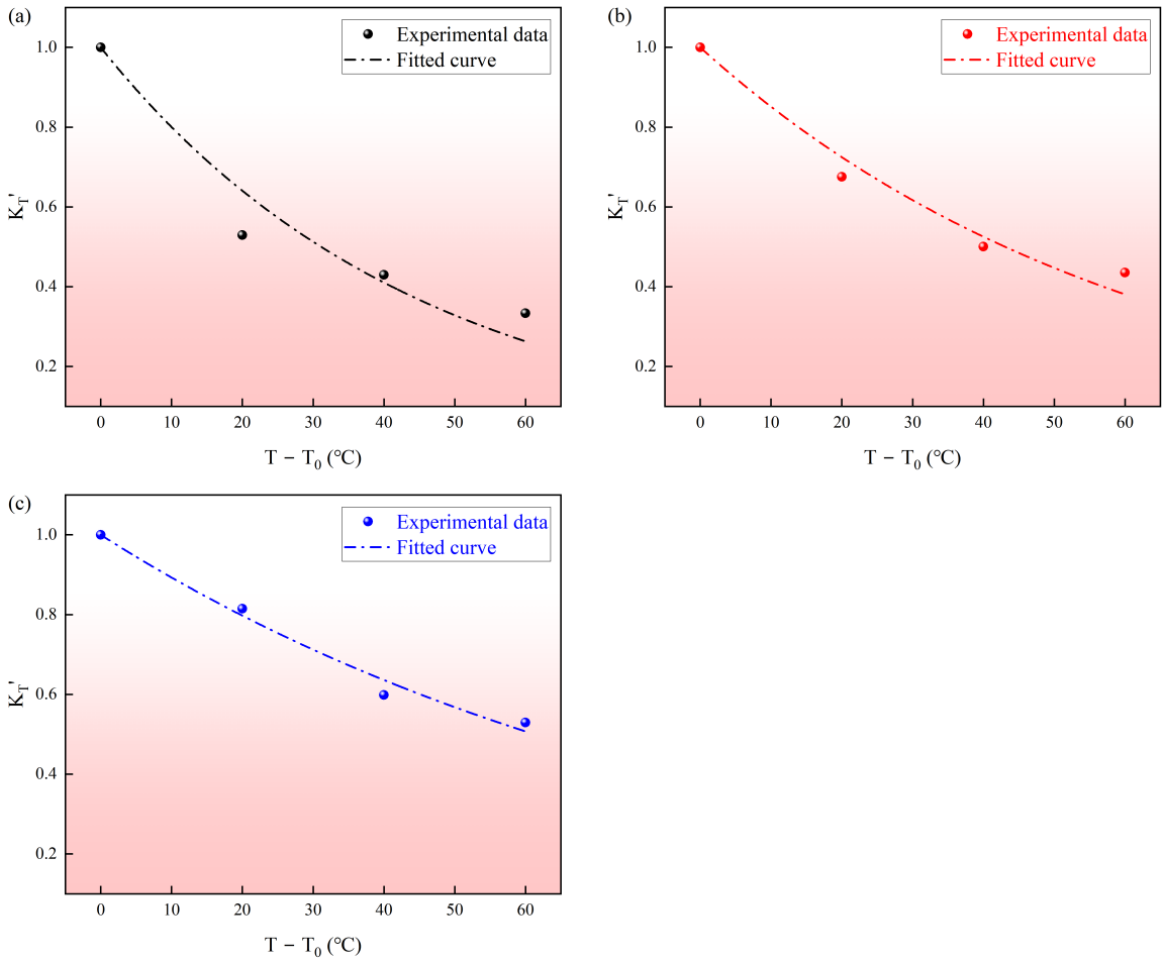


**Figure 9.** Exponential fitting of normalized permeability ($K_T'$) versus temperature for the Middle core under different effective stresses: (**a**) 15 MPa; (**b**) 25 MPa; and (**c**) 35 MPa. The progressive flattening of the fitted curves at higher stress levels illustrates the mechanical 'passivation' of the thermal response as compliant conduits are pre-closed by effective stress.

**Table 6.** Fitted parameters of the exponential temperature-sensitivity model at different effective stresses.

| Sample | Effective Stress (MPa) | Model Form | $D$ (°C$^{-1}$) | $R^2$ |
|---|---|---|---|---|
| North | 15 | $K_T' = \exp[-D(T - T_0)]$ | 0.0229 ± 0.0026 | 0.9534 |
| | 25 | | 0.0160 ± 0.0006 | 0.9938 |
| | 35 | | 0.0125 ± 0.0008 | 0.9797 |
| Middle | 15 | | 0.0223 ± 0.0030 | 0.9323 |
| | 25 | | 0.0161 ± 0.0013 | 0.9685 |
| | 35 | | 0.0113 ± 0.0006 | 0.9842 |
| South | 15 | | 0.0189 ± 0.0028 | 0.9004 |
| | 25 | | 0.0128 ± 0.0013 | 0.9383 |
| | 35 | | 0.0075 ± 0.0003 | 0.9915 |

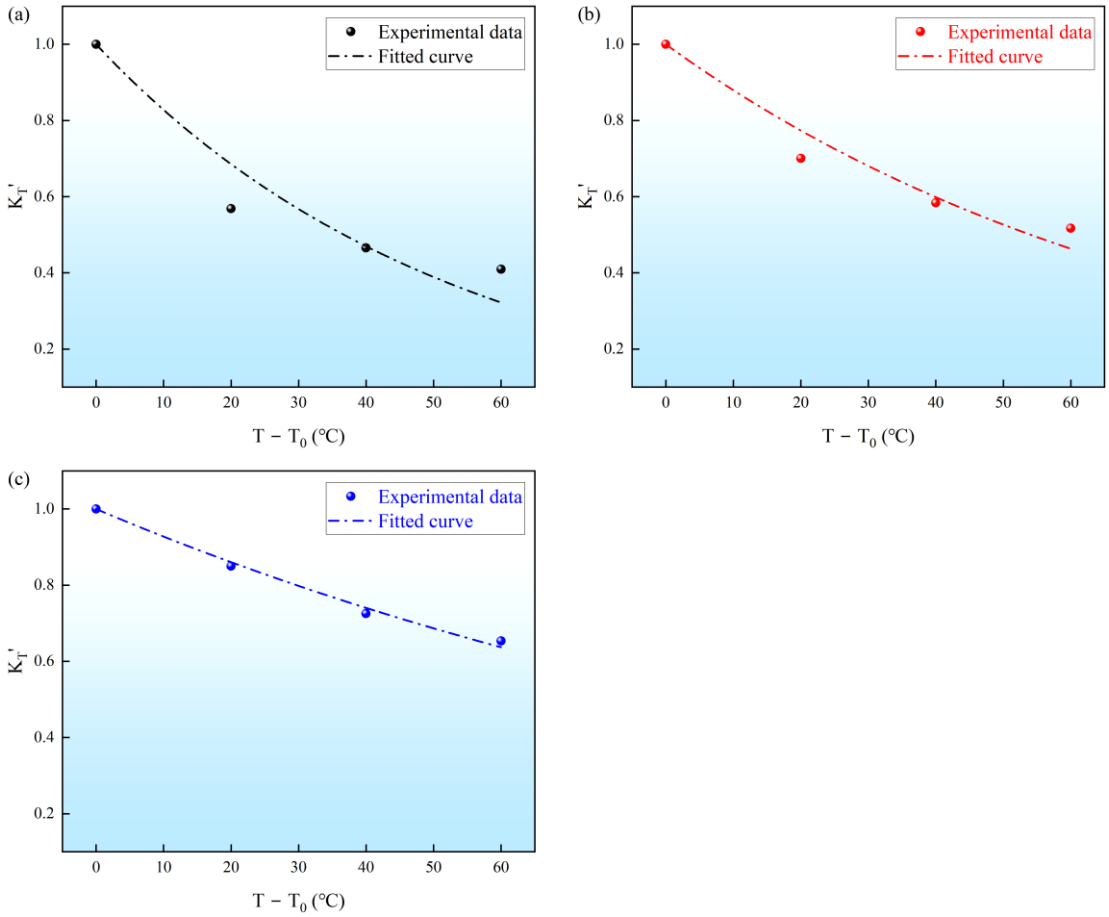


**Figure 10.** Exponential fitting of normalized permeability ($K_T'$) versus temperature for the South core under different effective stresses: (**a**) 15 MPa; (**b**) 25 MPa; and (**c**) 35 MPa. The progressive flattening of the fitted curves at higher stress levels illustrates the mechanical 'passivation' of the thermal response as compliant conduits are pre-closed by effective stress.

### *4.4. Exponential Permeability Model Under Coupled Temperature and Stress Conditions*

To represent the combined effects of effective stress and temperature within a unified framework, combining Equations (7) and (8) under the separability assumption gives:

$$K' = \exp[-C(\sigma - \sigma_0) - D(T - T_0)] \quad (9)$$

where $C$ (MPa$^{-1}$) and $D$ (°C$^{-1}$) are the stress-related and temperature-related exponential decay parameters. Equation (9) follows the separability assumption stated in Section 4.1 and does not include an explicit cross-term such as $\left(\sigma_{eff} - \sigma_0\right)(T - T_0)$.

The fitted parameters of the coupled model for the three specimens are listed in Table 7. The fitted $C$ values are approximately 0.038–0.046 MPa$^{-1}$, and the fitted $D$ values are approximately 0.016–0.020 °C$^{-1}$, with $R^2$ ranging from 0.878 to 0.929. This indicates that, within the effective stress range of this study (15–35 MPa), a 10 MPa increase in effective stress leads to a permeability reduction of roughly 32–37%. Within 20–80 °C, if effective stress is held constant, a 10 °C increase in temperature reduces permeability by about 15–18%.

**Table 7.** Fitted parameters of the coupled model for the three specimens based on Equation (9).

| Sample | Model Form | $C$ (MPa$^{-1}$) | $D$ (°C$^{-1}$) | $R^2$ |
|---|---|---|---|---|
| North | $K' = \exp[-C(\sigma - \sigma_0) - D(T - T_0)]$ | $0.0459 \pm 0.0039$ | $0.0203 \pm 0.0017$ | 0.9289 |
| Middle | | $0.0384 \pm 0.0037$ | $0.0194 \pm 0.0017$ | 0.9152 |
| South | | $0.0376 \pm 0.0039$ | $0.0160 \pm 0.0017$ | 0.8776 |

### *4.5. Model Validation and Error Analysis*

Using the fitted exponential model Equation (9), the normalized permeability of each specimen under different $\left(\sigma_{eff}, T\right)$ is predicted. To evaluate the model performance, the relative error is introduced:

$$\delta = \frac{\left|K'_{pred} - K'\right|}{K'} \times 100\% \tag{10}$$

where $K'_{pred}$ and $K'$ are the modeled and measured normalized permeability. For each specimen, the relative errors $\delta$, the mean relative error $\delta_{mean}$, the maximum relative error $\delta_{\max}$ and the 80th percentile of the relative error $\delta_{80}$ are summarized in Tables 8–10.

The error statistics in Tables 8–10 provide insight into the model's reliability. The mean relative error of approximately 11–12% for all specimens suggests that the parsimonious separable form is sufficient for capturing the primary trends of permeability evolution. However, it is noted that the maximum relative errors (up to 39%) typically occur at the lowest permeability values (e.g., 80 °C and 35 MPa). This is because, as absolute permeability approaches the reservoir's lower limit, even small numerical residuals result in high relative percentages. Despite these localized deviations, the 80th percentile of errors remains within a narrow band (22–24%), confirming the model's overall consistency for engineering applications.

**Table 8.** Error statistics of permeability model predictions for the North specimens.

| $T$ (°C) | $\sigma_{eff}$ (MPa) | $K'$ | $K'_{pred}$ | $\delta$ (%) | $\delta_{mean}$ (%) | $\delta_{max}$ (%) | $\delta_{80}$ (%) |
|---|---|---|---|---|---|---|---|
| 20 | 15 | 1.00 | 1.00 | 0.00 | 11.45 | 38.67 | 22 |
| 20 | 20 | 0.72 | 0.79 | 10.50 | | | |
| 20 | 25 | 0.58 | 0.63 | 9.80 | | | |
| 20 | 30 | 0.48 | 0.50 | 3.68 | | | |
| 20 | 35 | 0.40 | 0.40 | 0.27 | | | |
| 40 | 15 | 0.54 | 0.67 | 24.38 | | | |
| 40 | 25 | 0.41 | 0.42 | 1.50 | | | |
| 40 | 35 | 0.33 | 0.27 | 19.10 | | | |
| 60 | 15 | 0.43 | 0.44 | 3.64 | | | |
| 60 | 25 | 0.29 | 0.28 | 3.13 | | | |
| 60 | 35 | 0.23 | 0.18 | 21.94 | | | |
| 80 | 15 | 0.31 | 0.30 | 3.05 | | | |
| 80 | 25 | 0.24 | 0.19 | 20.59 | | | |
| 80 | 35 | 0.19 | 0.12 | 38.67 | | | |

**Table 9.** Error statistics of permeability model predictions for the Middle specimens.

| $T$ (°C) | $\sigma_{eff}$ (MPa) | $K'$ | $K'_{pred}$ | $\delta$ (%) | $\delta_{mean}$ (%) | $\delta_{max}$ (%) | $\delta_{80}$ (%) |
|---|---|---|---|---|---|---|---|
| 20 | 15 | 1.00 | 1.00 | 0.00 | 12.03 | 39.11 | 24 |
| 20 | 20 | 0.79 | 0.83 | 4.32 | | | |
| 20 | 25 | 0.64 | 0.68 | 6.61 | | | |
| 20 | 30 | 0.53 | 0.56 | 6.13 | | | |
| 20 | 35 | 0.45 | 0.46 | 3.26 | | | |
| 40 | 15 | 0.53 | 0.68 | 28.18 | | | |
| 40 | 25 | 0.43 | 0.46 | 7.11 | | | |
| 40 | 35 | 0.37 | 0.31 | 14.00 | | | |
| 60 | 15 | 0.43 | 0.46 | 7.14 | | | |
| 60 | 25 | 0.32 | 0.31 | 1.94 | | | |
| 60 | 35 | 0.27 | 0.21 | 20.63 | | | |
| 80 | 15 | 0.33 | 0.31 | 6.41 | | | |
| 80 | 25 | 0.28 | 0.21 | 23.52 | | | |
| 80 | 35 | 0.24 | 0.14 | 39.11 | | | |

**Table 10.** Error statistics of permeability model predictions for the South specimens.

| $T$ (°C) | $\sigma_{eff}$ (MPa) | $K'$ | $K'_{pred}$ | $\delta$ (%) | $\delta_{mean}$ (%) | $\delta_{max}$ (%) | $\delta_{80}$ (%) |
|---|---|---|---|---|---|---|---|
| 20 | 15 | 1.00 | 1.00 | 0.00 | 12.44 | 37.34 | 22 |
| 20 | 20 | 0.81 | 0.83 | 2.77 | | | |
| 20 | 25 | 0.65 | 0.69 | 6.10 | | | |
| 20 | 30 | 0.53 | 0.57 | 6.95 | | | |
| 20 | 35 | 0.44 | 0.47 | 6.91 | | | |
| 40 | 15 | 0.57 | 0.73 | 27.77 | | | |
| 40 | 25 | 0.45 | 0.50 | 9.96 | | | |
| 40 | 35 | 0.37 | 0.34 | 8.69 | | | |
| 60 | 15 | 0.47 | 0.53 | 13.22 | | | |
| 60 | 25 | 0.38 | 0.36 | 4.16 | | | |
| 60 | 35 | 0.32 | 0.25 | 22.30 | | | |
| 80 | 15 | 0.41 | 0.38 | 6.53 | | | |
| 80 | 25 | 0.33 | 0.26 | 21.43 | | | |
| 80 | 35 | 0.29 | 0.18 | 37.34 | | | |

## 5. Discussion

This chapter interprets the observed permeability evolution of fractured-porous carbonate rocks under coupled temperature and effective stress conditions. We first explain the stress-controlled exponential-type permeability decay and its microphysical origin, and then discuss why the temperature sensitivity is progressively attenuated by increasing effective stress within the investigated 20–80 °C conditions. Based on these observations, two full-path conceptual models are proposed for permeability evolution under effective-stress loading or temperature loading. Finally, we discuss the engineering relevance of the proposed exponential model and clarify its current applicability and limitations.

### *5.1. Stress-Controlled Permeability Decay and Full-Path Conceptual Model*

Table 7 shows that the fitted stress-related exponential decay parameter $C$ for the North, Middle, and South cores is 0.0459, 0.0384, and 0.0376 $MPa^{-1}$. This level of stress sensitivity is comparable to that reported for carbonate cores from the Malm geothermal reservoir in Germany [50] and is also consistent with observations in tight gas sandstones, where permeability decreases markedly as effective stress increases [51].

The exponential-type decay of permeability with increasing effective stress (Figure 7) can be interpreted as a non-uniform progressive closure of the fracture-pore network. Farahani et al. [52] suggested that flow pathways in fractured-porous rocks can be conceptualized as a network composed of highly compliant fractures (soft hydraulic units) connected with less compliant matrix pores (stiff hydraulic units). At relatively low effective stress, wide fractures and large-aperture channels accommodate most deformation. Their rapid closure and geometric rearrangement lead to a steep reduction in flow capacity. As effective stress increases further, the dominant fracture pathways become increasingly restricted, and the remaining flow is progressively carried by smaller pores and stiff contact areas. Consequently, additional stress increments cause smaller permeability changes, and the curve transitions to a gentler decay regime. This interpretation is consistent with the theoretical analysis of Zimmerman and Bodvarsson [43], who showed that the transmissivity of a single fracture decreases approximately with the cube of its mechanical aperture, revealing the microphysical origin of the macroscopic nonlinear stress sensitivity observed in this study.

Building on this interpretation, a conceptual model is proposed to describe permeability evolution along a broader effective-stress path (Figure 11). Two competing stages can be distinguished:

Stage I (mechanical compaction zone): When the effective stress has not yet reached the dilatancy threshold of the rock, the dominant mechanism is the mechanical closure of

pre-existing fractures and pores. Macroscopically, permeability decreases monotonically and rapidly with increasing effective stress. The stress range covered by the present experiments falls within this stage.

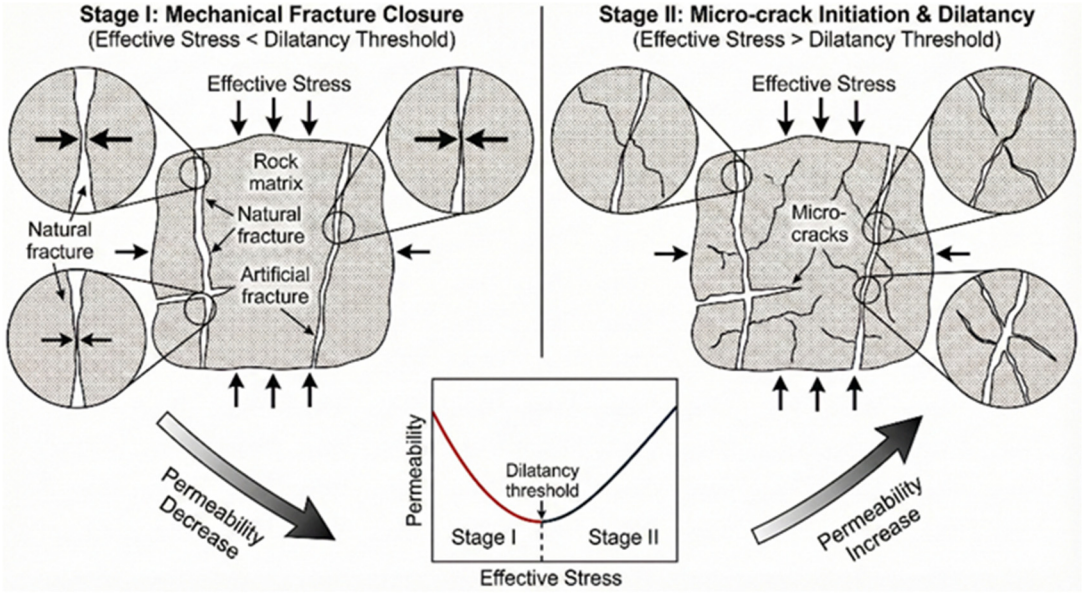


**Figure 11.** Conceptual model of permeability evolution in fractured-porous rocks under increasing effective stress, illustrating a fracture closure-dominated stage (Stage I) and a potential damage-induced micro-cracks stage (Stage II). The black arrows represent the application of effective stress, and the grey arrows indicate the overall trend of permeability evolution (decrease or increase).

Stage II (damage-induced dilatancy zone): If the effective stress continues to increase beyond the rock's dilatancy threshold, micro-crack initiation and propagation are triggered. As experimentally demonstrated by Zoback and Byerlee [53], microcrack dilatancy in the vicinity of the failure stress can cause a substantial increase in permeability, potentially exceeding initial values by several times, due to the formation of new flow channels. While our current data reside strictly within the mechanical compaction regime (Stage I), this inclusion of Stage II provides a comprehensive roadmap for reservoir behavior under extreme stress loading.

This model captures the entire nonlinear competitive evolution from "mechanical fracture closure" to "micro-crack initiation and dilatancy" and provides a theoretical framework for understanding reservoir behavior under more extreme loading conditions.

### *5.2. Temperature Sensitivity of Permeability Under Effective-Stress Regulation and Full-Path Conceptual Model*

From a mechanistic perspective, the maximum temperature in this study is 80 °C, which is well below the threshold for extensive thermal cracking commonly reported in heating-induced fracturing experiments (typically 200–300 °C) [22,54]. Therefore, within 20–80 °C, the observed permeability reduction is mainly attributed to thermoelastic deformation of the rock skeleton and microstructural rearrangement driven by mismatched thermal expansion among mineral constituents. When pre-existing fractures are not fully closed, heating tends to impose additional compression on relatively wide fracture segments, whereas the geometric adjustment of pore throats and smaller fractures is comparatively limited; as a result, the effective flow channels shrink without generating new fracture surfaces. Consistent behaviors have been reported in temperature-stress-permeability experiments on sandstones and granites, where permeability commonly decreases slowly with temperature at low to intermediate temperatures and increases sharply only after

pervasive thermal cracking develops at higher temperatures [23,49,54,55]. This indicates that the present experiments primarily capture the stage dominated by thermoelastic expansion-compression rather than thermal cracking.

As shown in Figure 6b–d, the temperature-caused permeability reduction is stronger at low effective stress and becomes progressively weaker at higher effective stress. For example, at $\sigma_{eff}$ = 15 MPa, heating from 20 to 80 °C reduces permeability by roughly 60% for the North, Middle, and South cores, whereas at $\sigma_{eff}$ = 35 MPa the reduction is only about 30%. The experimental results provide a clear quantitative link between mechanical confinement and the attenuation of temperature sensitivity. Specifically, as shown in Table 6 and Figure 12, the temperature-related decay parameter $D$ drops by approximately 45.4% to 60.3% across the three specimens as the effective stress increases from 15 to 35 MPa. This systematic reduction in $D$ quantifies the passivation effect: at 15 MPa, the unclosed and compliant fractures maximize the permeability response to thermoelastic expansion, leading to higher sensitivity. However, as the effective stress triples to 35 MPa, the mechanical pre-closure of these primary conduits, which accounts for an initial 55–60% permeability loss (Section 3.2), leaves a stiffer skeleton dominated by less-compressible matrix pores. This transition from fracture-dominated to matrix-dominated flow significantly weakens the capacity of mineral expansion to further restrict the seepage pathways, thereby numerically reducing the temperature sensitivity of the bulk rock. A comparable "passivation" of temperature sensitivity at higher effective stresses has also been reported for Beishan granite and several Chinese sandstones [23,55].

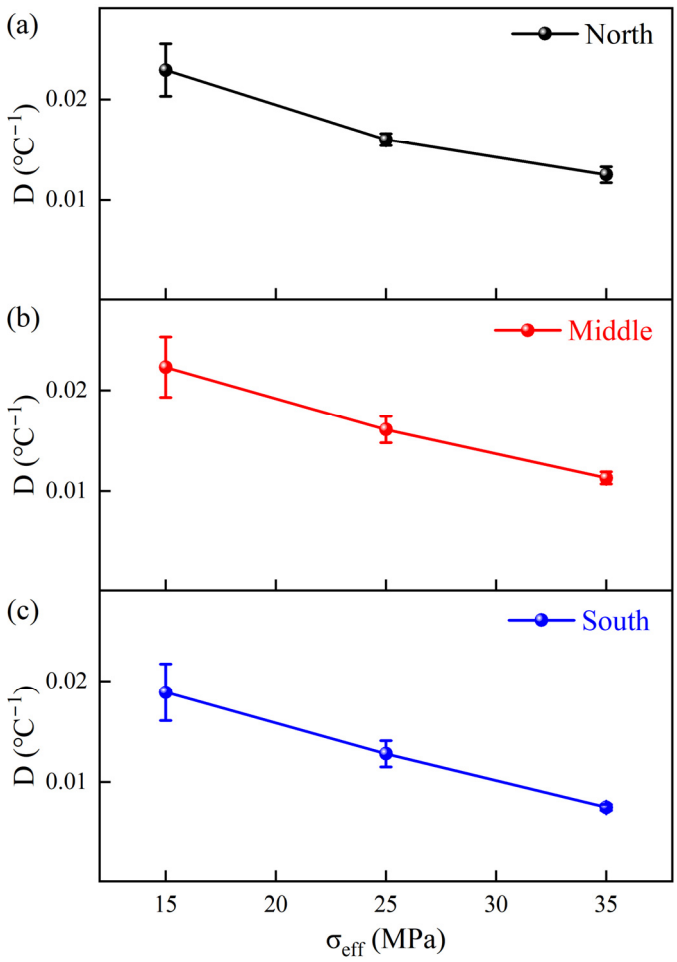


**Figure 12.** Fitted temperature-related exponential decay parameter $D$ under different effective stress for the (**a**) North, (**b**) Middle, and (**c**) South cores. Error bars denote the standard error of $D$ obtained from exponential fitting.

Based on the experimental results and rock thermophysical theory, we propose a full path mechanistic model for permeability evolution under temperature loading (Figure 13). The model comprises two competing stages.

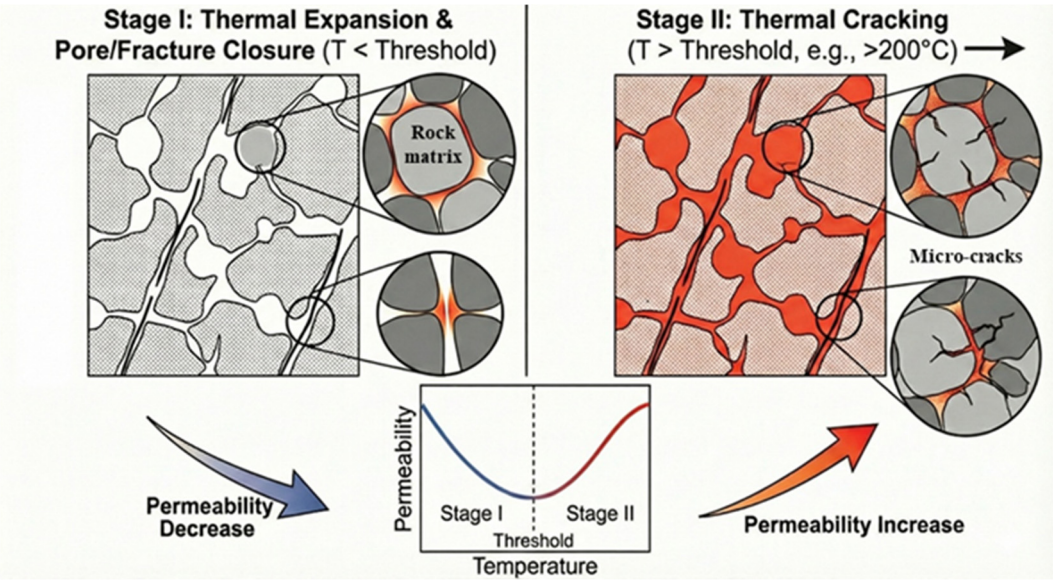


**Figure 13.** Conceptual model for the full path permeability evolution under temperature loading. Stage I (20–80 °C in this study) is dominated by thermoelastic expansion and progressive closure of pores and fractures. Stage II (typically > 200 °C) is dominated by thermal cracking, which may enhance permeability and reverse the overall trend.

Stage I (thermal expansion induced permeability reduction zone): Within the operational temperature conditions of this study (20–80 °C), permeability decreases mainly because matrix minerals undergo thermoelastic expansion. Owing to mismatched thermal expansion among mineral constituents and the confinement imposed by external stresses, the expanding grains progressively encroach on pre-existing pore and fracture space, narrowing effective flow paths, especially relatively wide fractures. This mechanism provides a microphysical explanation for the exponential type permeability decay with increasing temperature observed here, and it represents the dominant response for XGS-UGS operating conditions.

Stage II (thermal cracking induced permeability enhancement zone): If temperature continues to rise beyond the thermal cracking threshold (typically > 200 °C) [22,54], thermally induced stresses may exceed intergranular cohesive strength, triggering intergranular microcrack initiation and the propagation of pre-existing fractures [49,54,55]. According to the study on carbonates by Yang et al. [56], increasing temperature leads to the progressive development of internal micro-fractures and a decrease in the elastic modulus. This real-time thermal cracking can enhance network connectivity and potentially reverse the permeability reduction trend. Although the temperatures in this study (20–80 °C) remain within the Stage I closure regime, the model reflects the well-documented thermo-mechanical evolution of carbonate reservoirs under higher thermal loads.

### *5.3. Limitations*

The 1:1 comparison between modeled and measured values, together with the 80% error band, are presented in Figure 14, which indicates a systematic bias of the model: in the range $K'$ = 0–0.4 (usually corresponding to high temperatures and high effective stresses), most predicted values fall below the 1:1 line (slight underestimation), whereas in the range $K'$ = 0.4–1.0 (corresponding to low temperatures and low effective stresses), the model tends

to overestimate permeability. This suggests that the actual temperature-stress coupling does not strictly follow a single exponential law with constant parameters, but exhibits piecewise nonlinearity: at low temperatures and low effective stresses, fractures are only partially closed and highly compliant; as temperature and effective stress increase, most fractures become nearly closed, additional load is mainly borne by matrix pores, and permeability changes become less pronounced. Therefore, an exponential model with constant $C$ and $D$ cannot fully capture the "initially steep then gradually gentle" curve shape. To further mitigate this systematic bias, future model development could benefit from adopting a piecewise parameterization or a stress-dependent formulation (e.g., $C\left(\sigma_{eff}\right)$ and $D\left(\sigma_{eff}\right)$). Such an approach would allow the decay parameters to evolve with the mechanical state of the rock: using higher sensitivity values in the low-stress regime to represent compliant fracture closure and lower values at high stresses to reflect the dominance of stiffer matrix pores. By explicitly accounting for the varying stiffness of the hydraulic units, such refinements could effectively reduce the current overestimation at high normalized permeability values and the underestimation at low values. In addition, Equation (9) assumes separability and does not include higher-order coupling terms; at higher temperatures and larger stresses, or in scenarios involving pronounced dissolution-precipitation and thermally induced fracture development [57], a separable exponential form may be insufficient to describe strongly nonlinear coupling. With broader experimental data covering wider conditions and controlling factors, more flexible constitutive forms incorporating explicit cross terms could be developed to further refine and generalize the present exponential model. While more complex constitutive forms incorporating explicit cross-terms could potentially reduce residuals further, the current separable model provides a robust balance between mathematical simplicity and predictive accuracy. The consistency shown in the 1:1 comparison (Figure 14) confirms that for fractured-porous carbonates in XGS-UGS, the independent parameterization of $C$ and $D$ is sufficient to reproduce the overall permeability trends across diverse temperature and stress conditions.

Another limitation is the reliance on macroscopic seepage measurements to infer micro-scale deformation processes. While the current flow-based results accurately quantify the hydraulic aperture response, which is essential for evaluating UGS injectivity and deliverability, they do not provide direct visual evidence of the internal geometric evolution. High-resolution micro-CT imaging would be invaluable for visualizing localized fracture closure, asperity damage, and thermally induced micro-cracking under loading. However, performing high-resolution in-situ scans at the investigated moderate temperatures and high stresses (80 °C; 35 MPa) remains a significant technical challenge. Moreover, ex-situ measurements may introduce stress-release artifacts that alter the fracture contact state. Consequently, microstructural changes are currently absorbed into the fitted exponential parameters rather than being parameterized explicitly. Future research incorporating specialized in-situ CT scanning systems will be prioritized to provide more rigorous geometric validation for the proposed thermo-mechanical coupling mechanisms.

Furthermore, the use of a single throughgoing artificial fracture to represent the flow path (Section 2.1) introduces certain scale-dependent simplifications. While this approach ensures experimental repeatability and allows for clear quantification of thermo-mechanical coupling mechanisms, it simplifies the multi-scale nature of natural fracture networks. In natural reservoirs, fractures exhibit diverse orientations relative to the core axis, varying surface roughness, and heterogeneous mineral infillings (e.g., calcite or clay). These features not only define the initial seepage capacity but also significantly influence the local mechanical stiffness and thermal expansion response of the rock skeleton. Additionally, natural fractured specimens are often susceptible to structural damage during the high-precision machining process, making it technically challenging to prepare high-quality

samples that meet strict laboratory standards. Furthermore, while the axial orientation of the artificial fractures maximizes the initial seepage capacity of the core plugs, it does not account for the tortuosity and connectivity losses inherent in multi-scale fracture networks. Consequently, when extrapolating these findings to field-scale simulations, the proposed model should be viewed as a fundamental characterization of the 'hydraulic unit' response, which must be coupled with reservoir-scale geological models to account for the structural complexity and network-scale amplification of thermo-mechanical effects. Despite these simplifications, the proposed exponential parameters provide a consistent baseline for characterizing the response of primary seepage conduits in the XGS-UGS, serving as a critical input for upscale multiphysics simulations.

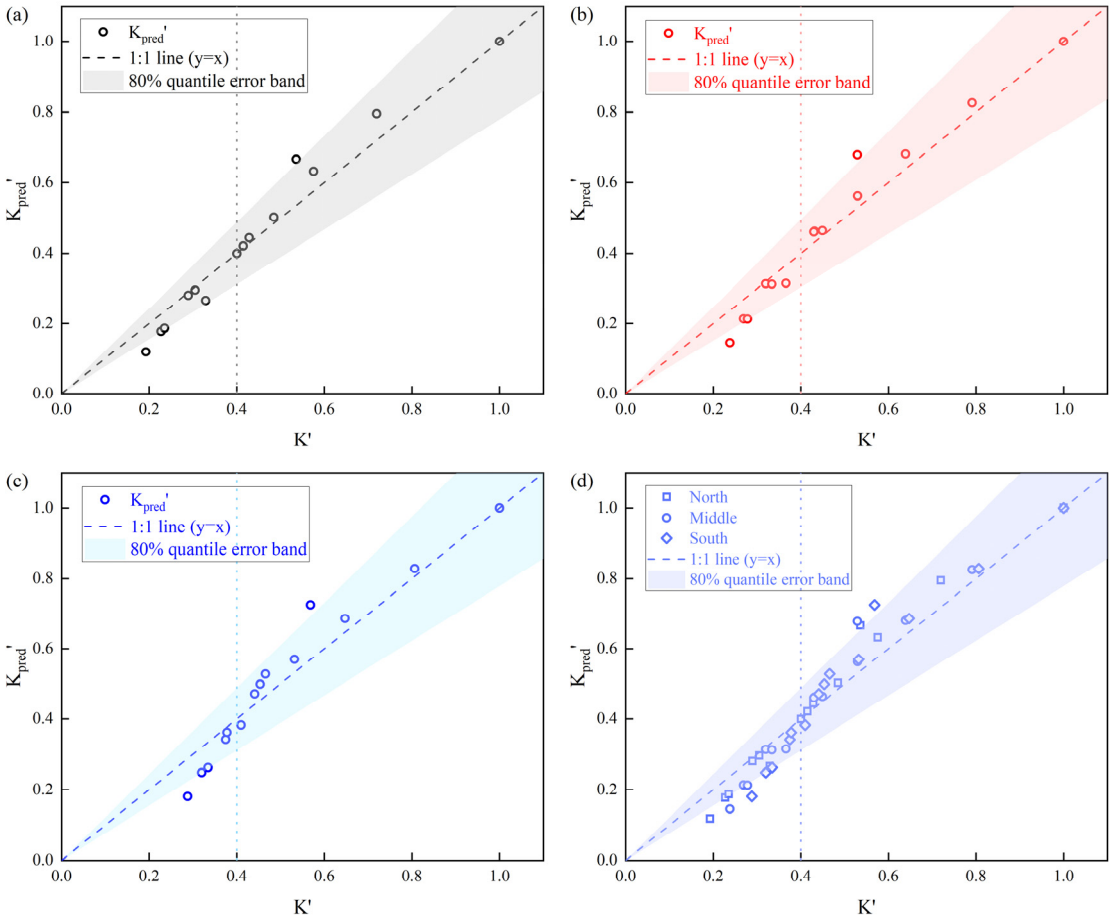


**Figure 14.** 1:1 comparison between modeled and measured normalized permeability under coupled temperature and stress conditions. The dashed line indicates $K'_{pred} = K'$; the shaded region denotes the 80th percentile error band. (**a**) North core; (**b**) Middle core; (**c**) South core; (**d**) combined data from all three cores.

The transition from a single laboratory-scale fracture to a complex reservoir-scale network can be achieved through the equivalent permeability ($k_{eq}$) concept. In this framework, the laboratory-derived parameters $C$ and $D$ serve as the fundamental constitutive response for the individual hydraulic conduits. When integrated into Discrete Fracture Network (DFN) or equivalent continuum models, the macroscopic permeability of a reservoir grid block can be expressed as an assembly of these responsive units. As the effective stress and temperature evolve during UGS operations, the aperture of each fracture within the network follows the calibrated exponential decay, collectively driving the evolution of the field-scale equivalent permeability. However, it is important to note that network-scale connectivity and the cooperative deformation of fractured-vuggy clusters may introduce

additional nonlinearities. Therefore, reservoir-scale simulations should utilize these laboratory results as a calibrated baseline while accounting for broader statistical variations in the coefficients to address the impact of complex heterogeneity.

The sensitivity parameters $C$ and $D$ are intrinsically linked to the mechanical state of the rock skeleton. In actual UGS facilities, gas injection increases pore pressure and reduces effective stress, potentially enhancing the reactivity of compliant fractures to both mechanical loading and thermal expansion. If the pore-pressure term in Equation (2) is neglected under high-pressure injection conditions, the model would likely underestimate the rate of permeability recovery. Therefore, for engineering implementation, the exponential model (Equation (9)) should be coupled with a dynamic effective stress calculation that explicitly accounts for localized pore pressure variations.

It is also worth noting that while apparent gas permeability was used without Klinkenberg correction, the identified sensitivity trends remain robust. In the low-mD range of XGS-UGS carbonates, the magnitude of permeability decay caused by fracture closure and mineral thermal expansion far outweighs potential slip-flow deviations. This ensures that the derived exponential parameters ($C$ and $D$) accurately reflect the relative seepage response of the reservoir skeleton to operational fluctuations.

Another limitation of the current study is the use of monotonic loading paths to calibrate the exponential parameters $C$ and $D$. While these parameters successfully quantify the sensitivity of the reservoir skeleton to initial stress and temperature perturbations, actual UGS operations involve high-frequency cycles of gas injection and withdrawal. Previous studies have indicated that multi-cycle effective stress perturbations can cause irreversible structural damage to the pore-fracture network, leading to permeability hysteresis where the unloading path deviates from the loading path. Such hysteresis often leads to cumulative permeability loss as fracture asperities undergo non-elastic deformation or mechanical fatigue over time. Therefore, the values of $C$ and $D$ reported here (Table 7) specifically represent the loading-path behavior. While they provide a robust upper-bound estimate for permeability decay during initial reservoir adjustment, they may not fully capture the long-term rock fatigue or the partial recovery of flow channels under cyclic conditions. Future research incorporating long-term cyclic testing is needed to extend the exponential model into a full-cycle constitutive relation for UGS performance prediction.

Finally, it is essential to acknowledge the indicative nature of the derived exponential parameters. The ranges identified for the stress-related decay parameter $C$ (0.038–0.046 $MPa^{-1}$) and the temperature-related decay parameter $D$ (0.016–0.020 $°C^{-1}$) provide a calibrated baseline for the fractured-porous units within the XGS-UGS under the investigated conditions (20–80 °C; 15–35 MPa). These parameters are representative of the coupled thermo-mechanical response of the primary flow conduits; however, reservoir-scale simulations should account for broader statistical variations in these coefficients to fully address the impact of complex heterogeneity on long-term UGS deliverability.

### 5.4. Engineering Significance

Within the investigated range (20–80 °C and the tested effective-stress levels), the proposed exponential model offers a concise engineering-scale tool to quantify coupled temperature and stress effects and to compare sensitivity among cores or reservoir intervals using fitted parameters ($C$ and $D$) in a consistent manner. The identified sensitivity provides a mechanistic basis for understanding field-scale permeability fluctuations in UGS facilities. During the gas injection phase, the rising pore pressure reduces effective stress, and the injection of relatively cold gas typically leads to localized cooling near the wellbore. Our experimental results confirm that both of these thermo-mechanical shifts favor the recovery of flow conduits, which is consistent with field observations where reservoir permeability

is generally higher during injection than during the production phase. However, the macroscopic impact on well performance is governed by the synergistic coupling of the sensitivity parameters ($C$ and $D$) and the spatial extent (radius) of the stress and temperature disturbance zones. While extreme permeability variations are primarily concentrated in the near-wellbore region, they act as a dynamic skin factor that dictates the Injectivity Index. Incorporating these localized and cyclic effects into reservoir simulations allows for a more accurate prediction of deliverability evolution and operational optimization over the entire UGS service life, preventing over-optimistic forecasts that fail to account for localized thermo-mechanical seepage restriction.

To illustrate the practical impact of the proposed model on UGS operations, a representative case study was conducted based on the operating parameters of the XGS-UGS. This facility typically operates with pore pressures between 12 and 30 MPa and formation temperatures ranging from 30 to 60 °C. During a withdrawal phase, as the pore pressure decreases from 30 MPa to 12 MPa, the effective stress acting on the rock skeleton increases by approximately 18 MPa. Concurrently, geothermal heat transfer can cause the localized near-wellbore temperature to rise from the injection state (30 °C) to the formation equilibrium state (60 °C). According to the calibrated exponential model and the sensitivity parameters derived in this study ($C \approx 0.042$ MPa$^{-1}$ and $D \approx 0.019$ °C$^{-1}$), this coupled thermo-mechanical loading leads to a localized permeability reduction of approximately 73% within the primary seepage conduits during a single withdrawal cycle. Such a substantial decay acts as a dynamic skin effect that significantly constrains the well's deliverability index.

From an engineering perspective, the proposed constitutive model $K(\sigma, T)$ can be integrated into reservoir simulators through two primary pathways:

Direct Analytical Embedding: The exponential relation can be implemented as a dynamic multiplier within the simulator's constitutive subroutines. This allows the solver to update the permeability of each grid block at every time step based on the instantaneous local stress and temperature fields.

Multi-dimensional Lookup Tables: For commercial simulators with restricted constitutive flexibility, the model can generate a 2D lookup table ($K'$ vs $\sigma_{eff}$ and $T$). The simulator then utilizes bilinear interpolation to determine the effective permeability multiplier during predictive calculations.

By accounting for these localized cyclic variations, the proposed model provides a quantitative tool for optimizing injection-production schedules and ensuring the long-term deliverability of fractured-porous carbonate reservoirs.

## 6. Conclusions

Steady-state gas permeability tests were conducted on three fractured-porous carbonate cores from the XGS-UGS under coupled temperature and effective stress conditions (20–80 °C; 15–35 MPa). The main conclusions are as follows:

(1) Overall permeability reduction under coupled loading. Permeability decreases markedly with increasing effective stress and temperature within the investigated conditions. Varying a single factor (either temperature or effective stress) typically leads to an approximately 30–70% reduction, whereas their combined increase can produce a maximum reduction exceeding 80% for the tested cores.

(2) Hierarchy of controlling factors and stress regulation of temperature sensitivity. Exponential-type fittings indicate that permeability is primarily governed by effective stress, while temperature plays a secondary, regulating role. The stress-related exponential decay parameter $C$ (0.038–0.046 MPa$^{-1}$) is consistently higher than the temperature-related exponential decay parameter $D$ (0.016–0.020 °C$^{-1}$) for all three

cores. In addition, $D$ decreases systematically with increasing effective stress, demonstrating that temperature sensitivity is strongly modulated by the stress state because compliant fractures and larger pores are progressively pre-closed.

(3) Mechanistic interpretation and conceptual regimes. The stress-induced permeability decay can be interpreted as a non-uniform progressive closure of the fracture-pore network: rapid closure of compliant flow paths dominates at relatively low effective stress, followed by a gentler decay as flow becomes increasingly controlled by stiffer pores and contact areas. Within 20–80 °C, the observed temperature effect is mainly attributed to thermoelastic deformation and microstructural rearrangement that narrow existing flow channels, rather than pervasive thermal cracking. Conceptually, under more extreme effective-stress or temperature loading, microcracks may propagate and induce dilatancy, potentially enhancing permeability; however, the operating-relevant conditions examined here remain within a closure-dominated regime.

(4) Exponential model and applicability. A concise, physically interpretable exponential model was proposed to describe permeability evolution under coupled temperature-effective stress loading, showing good predictive performance within the investigated ranges (mean relative error on the order of 10%). The model can be implemented as a constitutive permeability module in multiphysics simulations to support injectivity/deliverability evaluation and operational optimization for XGS-UGS and other UGS sites with similar fractured-porous carbonate settings.

**Author Contributions:** Z.Z.: Conceptualization, Methodology, Formal analysis, Investigation, Data curation, Writing—original draft—review & editing. Q.G.: Conceptualization, Methodology, Validation, Resources, Formal analysis, Investigation, Data curation, Writing—review & editing, Funding acquisition. Y.W.: Conceptualization, Methodology, Validation, Formal analysis, Writing—review & editing. S.H.: Conceptualization, Methodology, Investigation, Data curation, Writing—review & editing. Y.Z.: Conceptualization, Methodology, Validation, Formal analysis, Writing—review & editing. L.L.: Conceptualization, Methodology, Validation, Formal analysis, Writing—review & editing. M.X.: Conceptualization, Methodology, Validation, Formal analysis, Writing—review & editing. J.W.: Conceptualization, Methodology, Validation, Formal analysis, Writing—review & editing. S.J.: Conceptualization, Methodology, Validation, Resources, Formal analysis, Investigation, Data curation, Writing—review & editing, Funding acquisition. All authors have read and agreed to the published version of the manuscript.

**Funding:** National Natural Science Foundation of China (Project Nos. U23B20160, 5217041034, and 42402248), $CO_2$ Enhanced Shale Gas Recovery and Sequestration by Numerical Thermal-Hydro-Mechanical-Chemical modelling (Grant No. 2023DQ02-0206) funded by PetroChina Research Institute of Petroleum Exploration & Development, and Chongqing Natural Science Foundation (Project No. CSTB2025NSCQ-GPX0718).

**Data Availability Statement:** The original contributions presented in this study are included in the article. Further inquiries can be directed to the corresponding author(s).

**Acknowledgments:** This research was funded by the National Natural Science Foundation of China (Project Nos. U23B20160, 5217041034, and 42402248), $CO_2$ Enhanced Shale Gas Recovery and Sequestration by Numerical Thermal-Hydro-Mechanical-Chemical modelling (Grant No. 2023DQ02-0206), and the Chongqing Natural Science Foundation (Project No. CSTB2025NSCQ-GPX0718).

**Conflicts of Interest:** Author Yan Wang and Limin Li were employed by the company Chongqing Xiangguosi Underground Gas Storage Company Limited. Author Yuchao Zhao was employed by the company Exploration and Development Research Institute, PetroChina Southwest Oil & Gasfield Company. The remaining authors declare that the research was conducted in the absence of any commercial or financial relationships that could be construed as a potential conflict of interest.

## References


1. Ma, X.H.; Zheng, D.W.; Wei, G.Q.; Ding, G.S.; Zheng, S.J. Development Directions of Major Scientific Theories and Technologies for Underground Gas Storage. *Nat. Gas Ind.* **2022**, *42*, 93–99. (In Chinese) [CrossRef]
2. Hu, Y.; Wang, M.Y.; Luo, L.; Li, L.X.; Peng, X.; Zhao, Z.H. Technical Basis and Development Idea for the Construction of "Gas Storage Capacity in Southwest China". *Nat. Gas Ind.* **2024**, *44*, 1–13. (In Chinese) [CrossRef]
3. Zheng, D.W.; Wanyan, Q.Q.; Zhao, K. Development Status and Prospect of Underground Natural Gas Storage in China. *Int. Pet. Econ.* **2025**, *33*, 37–45. (In Chinese) [CrossRef]
4. Liu, J.; Pei, J.; Wei, J.; Yang, J.; Xu, H. Development Status and Prospect of Salt Cavern Energy Storage Technology. *Earth Energy Sci.* **2025**, *1*, 159–179. [CrossRef]
5. Wei, G.Q.; Zheng, Y.L.; Qiu, X.S.; Sun, J.C.; Shi, L.; Lei, X. Geological Theory and Application of Underground Gas Storage in China. *Acta Pet. Sin.* **2019**, *40*, 1519–1530. (In Chinese) [CrossRef]
6. Sun, J.C.; Xu, H.C.; Wang, J.M.; Shi, L.; Li, C.; Tang, L.; Zhong, R. Injection–Production Mechanisms and Key Evaluation Technologies for Underground Gas Storages Rebuilt from Gas Reservoirs. *Nat. Gas Ind.* **2018**, *38*, 138–144. (In Chinese) [CrossRef]
7. Zheng, X.; Zhao, Y.C.; Zhao, Z.H.; Tang, H.Y.; Zhao, Y.L. Mechanism Investigation on In-Situ Stress Characteristics and Mechanical Integrity of Fracture-Cavity Carbonate Underground Gas Storage Reservoir. *Pet. Reserv. Eval. Dev.* **2024**, *14*, 814–824.
8. Zhao, Y.C.; Luo, Y.; Li, L.X.; Zhou, Y.; Li, L.M.; Wang, X. In-Situ Stress Simulation and Integrity Evaluation of Underground Gas Storage: A Case Study of the Xiangguosi Underground Gas Storage, Sichuan, SW China. *J. Geomech.* **2022**, *28*, 523–536. (In Chinese)
9. Gan, Q.; Song, H.; Elsworth, D.; Jia, S.; Chen, J.; Ma, F.; Li, Q.; Yang, Y.; Wang, X.; Dai, Z. Deep Learning-Enhanced Global Sensitivity Analysis for Uncertainty Quantification in THMC Coupled sc$CO_2$-EGS. *Energy* **2025**, *335*, 138086. [CrossRef]
10. Fan, Y.; Gao, X.P.; Ning, F. Seepage Law of Gas-Reservoir UGSs during Multi-Cycle Injection and Production. *Nat. Gas Ind.* **2023**, *43*, 103–111. (In Chinese) [CrossRef]
11. Sun, K.; Liu, H.; Leung, J.Y.; Wang, J.; Feng, Y.; Liu, R.; Kang, Z.; Zhang, Y. Impact of Effective Stress on Permeability for Carbonate Fractured-Vuggy Rocks. *J. Rock Mech. Geotech. Eng.* **2024**, *16*, 942–960. [CrossRef]
12. Gao, X.; Yang, J.; Han, H.; Peng, J.; Peng, H.; Yang, Z. Experimental Research on the Effect Caused by Effective Stress Change in Injection Production Capacity of Carbonate Reservoir. *Front. Earth Sci.* **2023**, *11*, 1101056. [CrossRef]
13. Yan, F.M.; Kang, Y.L.; Li, S.; Du, C.C.; Li, D.M. Simulated Experiment on Stress Sensitivity in Fractured-Vuggy Reservoir. *Nat. Gas Geosci.* **2010**, *21*, 489–493+507. (In Chinese)
14. Haghi, A.H.; Chalaturnyk, R.; Talman, S. Stress-Dependent Pore Deformation Effects on Multiphase Flow Properties of Porous Media. *Sci. Rep.* **2019**, *9*, 15004. [CrossRef]
15. Zivar, D.; Foroozesh, J.; Pourafshary, P.; Salmanpour, S. Stress Dependency of Permeability, Porosity and Flow Channels in Anhydrite and Carbonate Rocks. *J. Nat. Gas Sci. Eng.* **2019**, *70*, 102949. [CrossRef]
16. Mi, O.; Wang, Z.; Zhang, R.; Zhang, Z.; Zhang, B. Permeability Stress Sensitivity Effect and Evolution Model of Dual Medium in Tight Sandstone Reservoirs. *Measurement* **2026**, *259*, 119627. [CrossRef]
17. Gou, Y.; Sun, J.C.; Yang, Z.M.; Zhou, X.M. Permeability-Stress Sensitivity of Complex Lithology Reservoir and Its Effect on Gas Well Productivity. *Rock Soil Mech.* **2014**, *35*, 2535–2542. (In Chinese) [CrossRef]
18. Yang, Y.; Tao, L.; Yang, H.; Iglauer, S.; Wang, X.; Askari, R.; Yao, J.; Zhang, K.; Zhang, L.; Sun, H. Stress Sensitivity of Fractured and Vuggy Carbonate: An X-Ray Computed Tomography Analysis. *J. Geophys. Res. Solid Earth* **2020**, *125*, e2019JB018759. [CrossRef]
19. Pu, Z.; Tian, Y.; Fu, J.; Yang, Y.; Satea, A.; Xiao, Z.; Zhao, Y.; Zhang, L. Stress-Sensitive Porosity and Permeability in Carbonate Rocks for Underground Hydrogen Storage: A Digital Rock Simulation Study. *Int. J. Coal Sci. Technol.* **2025**, *12*, 55–71. [CrossRef]
20. Zheng, S.J.; Zheng, D.W.; Sun, J.C.; Li, C.; Wu, Z.D.; Zhu, Z.S.; Liu, X.S. Temperature-sensitivity of Underground Gas Reservoir Storage and Its Effect on Well Deliverability. *Pet. Geol. Exp.* **2022**, *44*, 365–372. (In Chinese) [CrossRef]
21. Zhu, S.N.; Zeng, D.Q.; Zhang, G.Q.; Jia, Y.W.; Yang, X.S.; Wang, D.D. Evaluation Method and Evolutionary Characteristics of Damaged Cap Rock Sealing Capacity in Gas Reservoir Type Underground Gas Storage under Multi-Cycle Injection-Production Conditions. *Nat. Gas Geosci.* **2024**, *35*, 2078–2090. (In Chinese)
22. Tomás, R.; Benavente, D.; Martínez-Ibáñez, V.; Garrido, M.E. How Do High Temperatures Affect Rock Properties? A Comprehensive Review of Experimental Thermal Effects and Underlying Mechanisms. *Eng. Geol.* **2025**, *357*, 108323. [CrossRef]
23. Wang, L.; Wu, Y.; Huang, Z.; Lin, J.; Wang, Y.; Zhang, W. Effects of Temperature and Confining Pressure on the Permeability of Beishan Granite from High-Level Radioactive Waste Disposal Repository. *Case Stud. Therm. Eng.* **2024**, *55*, 104111. [CrossRef]
24. Zhai, Z.; Li, K.; Bao, X.; Tong, J.; Yang, H.; Han, B. Experimental Studies on Influence of Temperature on Relative Permeability Curves in Sandstone Reservoirs. *Energy Explor. Exploit.* **2022**, *40*, 206–223. [CrossRef]
25. Wang, H.J. New Approach to the Thermal Properties of Carbonate Rocks in Geothermal Reservoirs: Molecular Dynamics Calculation and Case Studies. *Renew. Energy* **2022**, *198*, 861–871. [CrossRef]

26. Luo, X.; Zheng, Y.; Huang, P.; Yang, L.; Chen, X.; Ren, X.; Wang, G.; Wang, Y.; Wang, Z.; Li, X. Experimental Study of the Flow Mechanism of Deep Lacustrine Carbonate Reservoirs in the Yingxi Area of the Qaidam Basin. *Geofluids* **2022**, *2022*, 8328764. [CrossRef]
27. Huang, Z.; Zhou, X.; Wang, H.; Wang, Q.; Wu, Y.-S. Stress Sensitivity Analysis of Vuggy Porous Media Based on Two-Scale Fractal Theory. *Sci. Rep.* **2024**, *14*, 20710. [CrossRef]
28. *SL/T 264-2020*; Specifications for Rock Tests in Water Conservancy and Hydropower Engineering. China Water & Power Press: Beijing, China, 2020.
29. *GB/T 50266-2013*; Standard for Test Methods of Engineering Rock Masses. China Planning Press: Beijing, China, 2013.
30. *API RP 40*; Recommended Practices for Core Analysis. American Petroleum Institute: Washington, DC, USA, 1998.
31. *GB/T 29172-2012*; Practices for Core Analysis. Standards Press of China: Beijing, China, 2012.
32. Li, X.C.; Feng, Z.C.; Guo, J.Z.; Liang, Y.K.; Bai, J.; Wang, C. Study on Influence Laws of Temperature and Stress on Sandstone Permeability. *Coal Sci. Technol.* **2019**, *47*, 96–100. (In Chinese)
33. Bu, Y.S.; Yang, S.Q.; Huang, Y.H. Experimental Study on the Influence of Temperature and Damage Degree on the Permeability of Sandstone. *Eng. Mech.* **2021**, *38*, 122–130. (In Chinese)
34. Liu, J.F.; Ni, H.Y.; Pu, H.; Huang, B.X.; Yao, Q.L.; Mao, X.B. Test Theory, Method and Device of Gas Permeability of Porous Media and the Application. *Chin. J. Rock Mech. Eng.* **2021**, *40*, 137–146. (In Chinese)
35. Jia, C.J.; Wang, H.L.; Xu, W.Y.; Zuo, J.; Skoczylas, F. Study on Gas Permeation and Slippage Effects in Rock Mass of Underground Water-Sealed Cave. *Eng. Mech.* **2015**, *32*, 50–57. (In Chinese)
36. Hibi, Y.; Fujinawa, K.; Nishizaki, S.; Okamura, K.; Tasaki, M. Investigation for Necessity of Dispersivity and Tortuosity in the Dusty Gas Model for a Binary Gas System in Soil. *Soils Found.* **2010**, *50*, 143–159. [CrossRef]
37. Huber, M.L.; Perkins, R.A.; Lemmon, E.W. Reference Correlation for the Viscosity of Nitrogen from the Triple Point to 1000 K and Pressures up to 2200 MPa. *Int. J. Thermophys.* **2024**, *45*, 146. [CrossRef] [PubMed]
38. Sun, Y.Z.; Xie, L.Z.; He, B.; Gao, C.; Wang, J. Effects of Effective Stress and Temperature on Permeability of Sandstone from $CO_2$-Plume Geothermal Reservoir. *J. Rock Mech. Geotech. Eng.* **2016**, *8*, 819–827. [CrossRef]
39. Zhang, J.; Zhou, X.; Liu, X.; Fang, L.; Liu, Y.; Wang, Y. Deformation and Permeability of Fractured Rocks Using Fluid-Solid Coupling under Loading-Unloading Conditions. *J. Rock Mech. Geotech. Eng.* **2025**, *17*, 4889–4907. [CrossRef]
40. Jouini, M.S.; Alabere, A.O.; Alsuwaidi, M.; Morad, S.; Bouchaala, F.; Al Jallad, O.A. Experimental and Digital Investigations of Heterogeneity in Lower Cretaceous Carbonate Reservoir Using Fractal and Multifractal Concepts. *Sci. Rep.* **2023**, *13*, 20306. [CrossRef]
41. Shi, R.; Liu, J.; Wei, M.; Elsworth, D.; Wang, X. Mechanistic Analysis of Coal Permeability Evolution Data under Stress-Controlled Conditions. *Int. J. Rock Mech. Min. Sci.* **2018**, *110*, 36–47. [CrossRef]
42. Eggers, C.G.; Berli, M.; Accorsi, M.L.; Or, D. Deformation and Permeability of Aggregated Soft Earth Materials. *J. Geophys. Res. Solid Earth* **2006**, *111*, 2005JB004123. [CrossRef]
43. Zimmerman, R.W.; Bodvarsson, G.S. Hydraulic Conductivity of Rock Fractures. *Transp. Porous Media* **1996**, *23*, 1–30. [CrossRef]
44. Guo, X.; Zou, G.; Wang, Y.; Wang, Y.; Gao, T. Investigation of the Temperature Effect on Rock Permeability Sensitivity. *J. Pet. Sci. Eng.* **2017**, *156*, 616–622. [CrossRef]
45. Shi, J.; Durucan, S. Near-Exponential Relationship between Effective Stress and Permeability of Porous Rocks Revealed in Gangi's Phenomenological Models and Application to Gas Shales. *Int. J. Coal Geol.* **2016**, *154–155*, 111–122. [CrossRef]
46. Liang, Z.; Jiang, Z.; Wu, W.; Guo, J.; Wang, M.; Nie, Z.; Li, Z.; Xu, D.; Xue, Z.; Chen, R.; et al. Study and Classification of Porosity Stress Sensitivity in Shale Gas Reservoirs Based on Experiments and Optimized Support Vector Machine Algorithm for the Silurian Longmaxi Shale in the Southern Sichuan Basin, China. *ACS Omega* **2022**, *7*, 33167–33185. [CrossRef]
47. Liu, K.; Yin, D.Y.; Sun, Y.H. The Mathematical Model of Stress Sensitivities on Tight Reservoirs of Different Sedimentary Rocks and Its Application. *J. Pet. Sci. Eng.* **2020**, *193*, 107372. [CrossRef]
48. Wu, J.-B.; Yang, S.-L.; Li, Q.; Yang, K.; Huang, C.; Lv, D.-P.; Zhou, W. Micromechanism and Mathematical Model of Stress Sensitivity in Tight Reservoirs of Binary Granular Medium. *Pet. Sci.* **2024**, *21*, 1780–1795. [CrossRef]
49. Xu, Y.; Xiao, J.; Li, X.; Xia, K.; Peng, J. Experimental Study on the Permeability Evolution of Argillaceous Sandstone under Elevated Temperatures. *Eng. Geol.* **2023**, *313*, 106974. [CrossRef]
50. Bohnsack, D.; Potten, M.; Freitag, S.; Einsiedl, F.; Zosseder, K. Stress Sensitivity of Porosity and Permeability under Varying Hydrostatic Stress Conditions for Different Carbonate Rock Types of the Geothermal Malm Reservoir in Southern Germany. *Geotherm. Energy* **2021**, *9*, 15–74. [CrossRef]
51. Shar, A.M.; Mahesar, A.A.; Chandio, A.D.; Memon, K.R. Impact of Confining Stress on Permeability of Tight Gas Sands: An Experimental Study. *J. Petrol. Explor. Prod. Technol.* **2017**, *7*, 717–726. [CrossRef]
52. Farahani, M.; Aghaei, H.; Masoumi, H. Effect of Pore Type on Porosity, Permeability and Pore Volume Compressibility of Geological Formations Due to in-Situ Stress Change. *J. Pet. Sci. Eng.* **2022**, *218*, 110986. [CrossRef]

53. Zoback, M.D.; Byerlee, J.D. The Effect of Microcrack Dilatancy on the Permeability of Westerly Granite. *J. Geophys. Res.* **1975**, *80*, 752–755. [CrossRef]
54. Hu, J.; Xie, H.; Li, C.; Liu, G. Evolution Mechanism of Permeability of Hot Dry Rock under Coupled Effect of Thermal Fatigue and Seawater Interaction during Coastal Geothermal Development. *Renew. Sustain. Energy Rev.* **2024**, *189*, 114061. [CrossRef]
55. Ge, Z. Temperature and Pressure Effect on Permeability of Chinese Sandstone: A Review. *Acta Geodyn. Geomater.* **2018**, *15*, 289–296. [CrossRef]
56. Yang, W.D.; Wang, B.Q.; Yao, J.; Jing, W.J.; Zhang, X. Experimental study on mechanical properties of carbonate rocks under real-time high temperature and heat treatment under triaxial compression. *Chin. J. Rock Mech. Eng.* **2024**, *43*, 1347–1358. (In Chinese)
57. Jia, S.; Ma, F.; Yang, Z.; Zhou, Z.; Ling, H.; Lan, T.; Wang, W.; Tian, Y.; Thanh, H.V.; Soltanian, M.R.; et al. Retardation Factor Scaling for Contaminant Transport in Fractured Media. *Adv. Water Resour.* **2024**, *188*, 104709. [CrossRef]

**Disclaimer/Publisher's Note:** The statements, opinions and data contained in all publications are solely those of the individual author(s) and contributor(s) and not of MDPI and/or the editor(s). MDPI and/or the editor(s) disclaim responsibility for any injury to people or property resulting from any ideas, methods, instructions or products referred to in the content.